J. Fluid Mech. (1989), vol. 207, pp. 531–586
Printed in Great Britain

Lagrangian statistics from direct numerical simulations of isotropic turbulence

By P. K. YEUNG† AND S. B. POPE
Sibley School of Mechanical and Aerospace Engineering, Cornell University, Ithaca, NY 14853, USA

(Received 11 July 1988 and in revised form 4 April 1989)

A comprehensive study is reported of the Lagrangian statistics of velocity, acceleration, dissipation and related quantities, in isotropic turbulence. High-resolution direct numerical simulations are performed on 64^3 and 128^3 grids, resulting in Taylor-scale Reynolds numbers R_λ in the range 38–93. The low-wavenumber modes of the velocity field are forced so that the turbulence is statistically stationary. Using an accurate numerical scheme, of order 4000 fluid particles are tracked through the computed flow field, and hence time series of Lagrangian velocity and velocity gradients are obtained.

The results reported include: velocity and acceleration autocorrelations and spectra; probability density functions (p.d.f.'s) and moments of Lagrangian velocity increments; and p.d.f.'s, correlation functions and spectra of dissipation and other velocity-gradient invariants. It is found that the acceleration variance (normalized by the Kolmogorov scales) increases as $R_\lambda^{\frac{1}{2}}$ – a much stronger dependence than predicted by the refined Kolmogorov hypotheses. At small time lags, the Lagrangian velocity increments are distinctly non-Gaussian with, for example, flatness factors in excess of 10. The enstrophy (vorticity squared) is found to be more intermittent than dissipation, having a standard-deviation-to-mean ratio of about 1.5 (compared to 1.0 for dissipation). The acceleration vector rotates on a timescale about twice the Kolmogorov scale, while the timescales of acceleration magnitude, dissipation and enstrophy appear to scale with the Lagrangian velocity timescale.

1. Introduction

Lagrangian statistical quantities are of fundamental importance in the understanding of turbulence, especially turbulent dispersion and transport processes (Monin & Yaglom 1971). Unfortunately, Lagrangian statistics are extremely difficult to obtain experimentally because they require measurements following the random motion of fluid particles (which, by definition, move with the local instantaneous fluid velocity). Nevertheless, some useful data have been obtained by Snyder & Lumley (1971) and Shlien & Corrsin (1974). More recently, Sato & Yamamoto (1987) have measured Lagrangian velocity autocorrelations in grid turbulence, by tracking small tracer particles optically. However, higher-order quantities such as Lagrangian acceleration and velocity gradients are still inaccessible to reliable measurement.

In this paper we present Lagrangian statistics obtained from direct numerical simulations (DNS) of homogeneous isotropic turbulence, paying particular attention to the small scales. From the simulations we obtain time series of velocity and its

† Current Address: Mechanical Engineering, Queen's University, Kingston, Ontario, Canada K7L 3N6.

gradients following fluid particles. These times series are analysed to obtain many single-particle Lagrangian statistics of velocity, acceleration, dissipation, enstrophy and 'pseudo-dissipation' (defined in §3), including correlation functions, probability density functions (p.d.f.'s), structure functions and frequency spectra.

The significance of Lagrangian statistics to the problem of turbulent dispersion was recognized by Taylor (1921). More recently, dispersion in inhomogeneous turbulent flows has been studied using stochastic models for the velocity following a fluid particle (see e.g. Reid 1979; van Dop, Nieuwstadt & Hunt 1985; de Bass, van Dop & Nieuwstadt 1986 and Thompson 1987). Similar stochastic models have been used as a basis for the calculation of inhomogeneous turbulent flow fields (Pope 1983; Haworth & Pope 1986, 1987; and Anand, Pope & Mongia 1989). A recent advance in these stochastic models of Lagrangian velocity is to take account of internal intermittency (Haworth & Pope 1985; Pope 1988*a*, *b*). One objective of this study is to examine the Lagrangian time series obtained from DNS in relation to these stochastic models.

Sometimes called full turbulence simulations, the DNS approach is to obtain numerical solutions of the Navier–Stokes equation directly for the three-dimensional, fluctuating, velocity fields without any closure modelling. With continuing advances in supercomputers, DNS is being used to elucidate the physics of an increasing number of simple turbulent flows, mostly at moderate Reynolds numbers (e.g. Siggia 1981; Rogallo & Moin 1984; Kerr 1985; Rogers & Moin 1987). Pseudo-spectral methods (Hussaini & Zang 1987), pioneered by Orszag & Patterson (1972), are favoured because of their high accuracy. We use an adaptation of Rogallo's pseudo-spectral code for homogeneous turbulence (Rogallo 1981).

Direct numerical simulations offer great potential for computing Lagrangian statistics. Riley & Patterson (1974), who calculated velocity autocorrelations in decaying isotropic turbulence, were the first to exploit this possibility. Recently, Lee *et al.* (1987) used DNS to study Lagrangian two-point correlations and characteristic timescales. As discussed below, the Lagrangian results that we obtained earlier (Yeung & Pope 1987) are largely superseded by those presented in this paper.

The turbulence simulated is homogeneous and isotropic, without mean velocity gradients. It is made statistically stationary by forcing, i.e. by artificially adding energy to the low-wavenumber components of the velocity field. Compared to allowing the turbulence to decay, this practice has several advantages: stationary time series are more easily analysed; arbitrarily long-time series can (in principle) be obtained; specific initial conditions are not needed; the Reynolds number does not decay during the simulation; and the lengthscales of the turbulence do not grow. The disadvantage is that the large-scale motions are polluted by forcing† and differ – to some extent – from 'natural' turbulence. However, as Eswaran & Pope (1988*a*) have verified, provided an adequate separation of scales exists, the small scales, which are our primary focus of inquiry, are hardly affected. Consequently, one can be confident that the small-scale Lagrangian statistics, such as those of acceleration and dissipation, are close to those of unforced turbulence. For the velocity, the low-frequency statistics are affected by the forcing, while the high-frequency statistics are not appreciably affected. The forcing scheme used is a refinement of that developed and tested by Eswaran & Pope (1988*a*).

Lagrangian statistics can be extracted from the simulations because DNS provides complete information of the time-dependent Eulerian velocity field. The Lagrangian

† Even without forcing, the large-scale motions are significantly affected by the non-physical periodic boundary conditions.

time series are obtained by tracking fluid particles numerically, which is in turn dependent on the accurate calculation of fluid particle velocities by interpolation on the Eulerian grid network. The displacements at each time step are calculated from these velocities. Various quantities following the fluid particles can be similarly calculated and analysed statistically, taking an ensemble average over a sufficiently large number of particles. A particle-tracking algorithm has been devised recently by the authors (Yeung & Pope 1988) and has been shown to yield accurate results.

The Lagrangian statistics reported here are obtained from four 128^3 grid simulations, at Taylor-scale Reynolds numbers (R_λ) of 38, 63, 90 and 93, and from three 64^3 simulations with $R_\lambda = 38$, 54 and 59. On a 128^3 grid, Reynolds numbers significantly greater than 90 cannot be achieved without compromising the accuracy of the calculations – especially the accuracy of small-scale statistics.

Since some of our results show significant Reynolds-number dependence, it is important to appreciate the relationship between the highest Reynolds number in our simulations ($R_\lambda = 93$) and the Reynolds numbers obtained in laboratory turbulent flows. In grid-generated turbulence the Reynolds numbers are usually lower: at the first measurement station in the experiments of Warhaft & Lumley (1978) R_λ is about 55, and it decreases downstream. In the experiments of Comte-Bellot & Corrsin (1971), the equivalent value is $R_\lambda = 72$. In a turbulent boundary layer, R_λ increases with distance from the wall, and it can be estimated that $R_\lambda = 90$ is achieved at a distance of about 270 wall units – well into the logarithmic-law region. In a self-similar turbulent axisymmetric jet, the Reynolds number does not vary with axial distance. Based on empirical data (Schlichting 1979), it is estimated that $R_\lambda = 90$ is characteristic of a jet with a Reynolds number based on the pipe exit diameter of 7700. It may be seen, then, that $R_\lambda = 90$ is comparable with – in some cases higher than – the Reynolds numbers obtained in typical laboratory experiments.

We previously reported Lagrangian data from 64^3 simulations, for Reynolds numbers R_λ from 20 to 50 (Yeung & Pope 1987). A much wider range of results is given in the present paper. Besides the extension to higher Reynolds numbers made possible by having well-resolved Eulerian fields on 128^3 grids, the present study has incorporated several improvements in methodology. These include (*a*) a refined forcing scheme; (*b*) a better interpolation scheme having superior continuity properties; (*c*) a larger sample size through using more particles, and (*d*) a faster sampling rate giving more accurate high-frequency statistics.

This paper is organized as follows. The Eulerian numerical scheme is described in §2 where Eulerian spectra and scales used to characterize the simulated turbulence are presented. Section 3 gives an account of the methodology employed to extract and analyse Lagrangian data. The principal results are reported in §4. Attention is first focused on the statistics of acceleration to determine whether Reynolds-number similarity is observed under Kolmogorov (and other) scaling. Then the auto-correlations and frequency spectra of velocity and acceleration are presented. Stochastic models for Lagrangian velocity are best examined in terms of temporal velocity increments: this is done in §4.3. One- and two-time statistics of the acceleration magnitude, dissipation, enstrophy and pseudo-dissipation fluctuations following a fluid particle are presented in §4.4. Again, implications for stochastic models used to calculate turbulent flows are considered. Finally, in §4.5, we examine the relationship between Lagrangian and Eulerian time statistics through velocity autocorrelations and spectra, comparing with the predictions of the 'advection hypothesis' proposed by Tennekes (1975). Conclusions are summarized in §5. In the Appendix we discuss the statistical errors in the simulations.

2. The Eulerian simulation

2.1. *Numerical method*

The Navier–Stokes equation is solved numerically using the pseudo-spectral method developed by Rogallo (1981) for homogeneous turbulence. A detailed description of the algorithm is provided by Lee & Reynolds (1985).

The time-dependent Eulerian velocity field, $\boldsymbol{u}(\boldsymbol{x}, t)$, is represented on an equispaced grid of N^3 grid points which form a cubic computational domain of width L_0. The velocity field is continued periodically (i.e. $\boldsymbol{u}(\boldsymbol{x}+\boldsymbol{z}L_0, t) = \boldsymbol{u}(\boldsymbol{x}, t)$, where $\boldsymbol{z}$ is any integer vector), and consequently $\boldsymbol{u}(\boldsymbol{x}, t)$ has a finite Fourier representation. There are N^3 corresponding discrete nodes in wavenumber space. Let $\boldsymbol{k}$ be the wavenumber vector at a given node, and k be its magnitude. The lowest non-zero wavenumber, denoted by k_0, is $2\pi/L_0$. The components of $\boldsymbol{k}$ are integer multiples of k_0, ranging from $(1-\frac{1}{2}N)\ k_0$ to $(\frac{1}{2}N)\ k_0$. We denote by $\hat{\boldsymbol{u}}(\boldsymbol{k}, t)$ the complex Fourier (wavenumber) coefficients of the velocity at time t: i.e. $\hat{\boldsymbol{u}}(\boldsymbol{k}, t)$ is the discrete Fourier transform of $\boldsymbol{u}(\boldsymbol{x}, t)$.

For each wavenumber, the Fourier velocity $\hat{\boldsymbol{u}}$ evolves by

$$\frac{\mathrm{d}\hat{\boldsymbol{u}}}{\mathrm{d}t} = \hat{\boldsymbol{a}}[\hat{\boldsymbol{u}}(t)], \tag{1}$$

where $\hat{\boldsymbol{a}}$ (obtained from the Navier–Stokes equation) represents the velocity time derivative in wavenumber space and is dependent on $\hat{\boldsymbol{u}}$ at all $\boldsymbol{k}$. This (vector) equation is integrated in time by an explicit second-order Runge–Kutta method.

The numerical scheme used differs from Rogallo's in two aspects. First, there is a small, but essential, modification to the treatment of aliasing error. Second, the low-wavenumber modes are forced.

The essence of the pseudo-spectral method is that the velocity products (that arise, for example, in the convective term) are evaluated in physical space, and then transformed to wavenumber space. This avoids the costly evaluation of the products in physical space as convolutions in wavenumber space; but it introduces aliasing errors, which are reduced by a combination of truncation and phase-shifting techniques. In Rogallo's code, the phase shifts are chosen at random on each time step, so that the aliasing error on the predictor step almost cancels the error from the previous corrector step. This results in the grid being shifted in physical space by a different random amount on each time step. As stated by Yeung, Girimaji & Pope (1988), for our purposes it is essential instead to use the same phase shift (chosen randomly at the outset) on each time step. Otherwise, multi-time statistics would contain unacceptably large alias errors. Furthermore, this modification allows Eulerian time series to be collected by simply recording values at fixed grid points.

The basic forcing scheme used to maintain the turbulence energy against viscous decay has been thoroughly described and tested by Eswaran & Pope (1988*a*). For each non-zero wavenumber node $\boldsymbol{k}$ lying within the spherical shell of radius K_F (i.e. such that $0 < k \leqslant K_\mathrm{F}$), an artificial random term $\hat{\boldsymbol{a}}_\mathrm{F}(\boldsymbol{k}, t)$ is added on the right-hand side of (1). Two choices of K_F are used: $2\sqrt{2}k_0$, for which the total number of forced modes, N_F, is 92; and $\sqrt{2}k_0$, for which N_F is 18. In the work of Eswaran & Pope (1988*a*) (and of Yeung & Pope 1987), for each forced mode, $\hat{\boldsymbol{a}}_\mathrm{F}(\boldsymbol{k}, t)$ is specified as a complex vector-valued Uhlenbeck–Ornstein (UO) stochastic process (see e.g. Karlin & Taylor 1981).

The UO processes are continuous, but not differentiable in time. This characteristic is found to have adverse effects on the smoothness properties of the Lagrangian

velocity time series. To make the forcing acceleration once-continuously differentiable, we replace the UO process by the 'integrated' Uhlenbeck–Ornstein (IUO) process. A comprehensive account of the properties of the IUO process and its numerical implementation in the forcing scheme is given by Yeung *et al.* (1988). The parameters in the IUO process to be specified are: the integral timescale (T_F) of $\hat{\boldsymbol{a}}_F(\boldsymbol{k}, t)$, the ratio T_M^* of its microscale to its integral scale, and an amplitude rate parameter ϵ^* (the amplitude is $(\epsilon^*/T_F)^{\frac{1}{2}}$). Different Reynolds numbers can be attained by varying either the kinetic viscosity (ν) or the forcing parameters (T_F, ϵ^*, T_M^*). It is found that the change from UO processes to IUO processes has little effect on one-time Eulerian statistics, but that it is successful in removing high-frequency noise from the frequency spectra.

Eswaran & Pope (1988*a*) briefly review other forcing schemes, such as those used by Siggia (1981) and Kerr (1985). Recently, Hunt, Buell & Wray (1987) used a different scheme based on a steady non-uniform body-force field acting at the large scales. For the present purposes, the scheme used here is more satisfactory and more thoroughly tested than the others mentioned.

Numerical accuracy depends on both spatial and temporal resolution. The former requires that the small scales (characterized by the Kolmogorov lengthscale η) be well resolved by the Eulerian grid. In an N^3 simulation, the highest resolvable wavenumber, denoted as k_{max}, is the largest integer multiple of k_0 not exceeding $\sqrt{2}N/3k_0$: it is $30k_0$ and $60k_0$ for 64^3 and 128^3 grids, respectively. The spatial resolution of a simulation is determined by the dimensionless parameter $k_{max}\eta$ (Yeung & Pope 1987, 1988; Eswaran & Pope 1988*a*; Lee & Reynolds 1985).† In physical space this parameter can be understood through the approximate relation $\Delta x/\eta \approx 3/(k_{max}\eta)$, where Δx is the grid spacing. It is found that the value $k_{max}\eta = 1.0$ is adequate for low-order velocity statistics, but that a value of at least 1.5 is needed for higher-order quantities such as dissipation and derivative statistics. All of our simulations have $k_{max}\eta$ values of approximately 1.5 or greater.

A 64^3, $R_\lambda = 38$ simulation was performed with identical physical parameters to the 128^3, $R_\lambda = 38$ case, which resulted in the value of $k_{max}\eta$ being 1.5 on the 64^3 grid (but 3.0 on the 128^3 grid). A comparison of the results from these two simulations is used to assess the error due to finite spatial resolution.

Before fluid particles are introduced, the Eulerian velocity field is allowed to evolve from some initial condition towards a statistically stationary state. The fluid particles are then tracked for a time T, during which Eulerian and Lagrangian statistical data are sampled at regular intervals for subsequent analysis. The accuracy of the time integration is determined by the time step Δt, or by the Courant number C. (The Courant number is defined by $C \equiv U_{max}\Delta t/\Delta x$, where U_{max} is the maximum (over all grid nodes) of the sum of the absolute values of the three velocity components.) The time-stepping error is generally negligibly small if C is kept below 0.5 (see Yeung & Pope 1988). However, to facilitate the time-series analysis, a fixed time step is chosen for the averaging time T. Thus, we stipulate $C = 0.5$ in the presimulation phase; but after reaching stationarity, a fixed value of Δt is chosen such that the Courant number remains near the range 0.4–0.5. (For one run (64^3, $R_\lambda = 38$) the conservative value $C = 0.25$ was used.)

† In Lee & Reynolds (1985), k_{max} is equivalent to the 'cutoff' wavenumber k_c.

	$R_\lambda = 38$	$R_\lambda = 38$	$R_\lambda = 54$	$R_\lambda = 59$	$R_\lambda = 63$	$R_\lambda = 90$	$R_\lambda = 93$
N	64	128	64	64	128	128	128
K_F/k_0†	$2\sqrt{2}$	$2\sqrt{2}$	$\sqrt{2}$	$\sqrt{2}$	$2\sqrt{2}$	$\sqrt{2}$	$\sqrt{2}$
ν	0.025	0.025	0.0158	0.0158	0.0105	0.006546	0.006546
u'	1.549	1.582	1.235	1.276	1.637	1.274	1.356
$\langle\epsilon\rangle$	2.501	2.651	0.770	0.775	2.673	0.780	0.893
τ_ϵ	1.446	1.420	3.001	3.184	1.510	3.174	3.099
T_e/τ_ϵ	0.507	0.534	0.367	0.406	0.407	0.343	0.297
T/τ_ϵ	4.84	2.84	3.60	3.39	2.38	1.89	1.94
T/T_e	9.55	5.32	9.81	8.35	5.85	5.51	6.53
τ_η/τ_ϵ	0.069	0.068	0.048	0.045	0.041	0.029	0.028
$\Delta t/\tau_\eta$	0.025	0.012	0.042	0.042	0.024	0.027	0.029
$k_0\eta$	0.0500	0.0493	0.0478	0.0476	0.0257	0.0247	0.0237
$k_{max}\eta$	1.50	2.96	1.43	1.43	1.54	1.48	1.42
v_η/u'	0.323	0.320	0.269	0.261	0.250	0.210	0.204
S_ϵ	0.540	0.550	0.524	0.513	0.516	0.526	0.512
$L_1/\frac{1}{2}L_0$	0.362	0.383	0.434	0.528	0.321	0.448	0.398
L_1/L_2	2.27	2.35	1.87	2.32	2.50	2.08	1.69
Λ/L_1	‡	‡	0.993	0.867	0.894	0.922	1.005
λ/L_1	0.536	0.500	0.504	0.437	0.399	0.326	0.359
η/L_1	0.044	0.041	0.035	0.029	0.025	0.018	0.019
L_e/L_1	2.42	2.29	3.35	3.02	3.01	3.55	4.12

† The other forcing parameters are the same for all cases listed here: $T_F = 0.6369$, $\epsilon^* = 0.01306$, $T_M^* = 0.4$.

‡ not recorded.

TABLE 1. Forcing parameters and Eulerian flow variables

2.2. *Flow parameters*

For each of the simulations, the input parameters and principal Eulerian statistics are given in table 1. The turbulent kinetic energy $\frac{1}{2}q^2$, and the r.m.s. velocity u', are obtained from the Eulerian velocity field by

$$q^2 = 3u'^2 = \langle u_i u_i \rangle. \tag{2}$$

From q^2 and the mean dissipation rate

$$\langle\epsilon\rangle = \tfrac{1}{2}\nu\left\langle\left(\frac{\partial u_i}{\partial x_j}+\frac{\partial u_j}{\partial x_i}\right)\left(\frac{\partial u_i}{\partial x_j}+\frac{\partial u_j}{\partial x_i}\right)\right\rangle, \tag{3}$$

we form the timescale $\tau_\epsilon \equiv \frac{1}{2}q^2/\langle\epsilon\rangle$ and the lengthscale $L_\epsilon \equiv (\frac{1}{2}q^2)^{\frac{3}{2}}/\langle\epsilon\rangle$. The expectations (indicated by angled brackets) in the definitions of q^2 and $\langle\epsilon\rangle$ (equations (2) and (3)) are estimated by averaging over space and time.

In isotropic turbulence, the Taylor microscale λ is related to the mean dissipation rate $\langle\epsilon\rangle$ by

$$\langle\epsilon\rangle = 15\nu u'^2/\lambda^2, \tag{4}$$

a relationship† we use to determine λ, and hence to obtain the Taylor-scale Reynolds number $R_\lambda \equiv u'\lambda/\nu$. The Kolmogorov length, time and velocity scales are defined as usual by $\eta = (\nu^3/\langle\epsilon\rangle)^{\frac{1}{4}}$; $\tau_\eta = (\nu/\langle\epsilon\rangle)^{\frac{1}{2}}$; and, $v_\eta = (\nu\langle\epsilon\rangle)^{\frac{1}{4}}$.

The two-point velocity correlation tensor (with separation vector $\boldsymbol{r}$) is defined as

$$R_{ij}(\boldsymbol{r}) = \langle u_i(\boldsymbol{x})\, u_j(\boldsymbol{x}+\boldsymbol{r})\rangle. \tag{5}$$

† In fact, we obtain a Taylor microscale for each component of velocity variance, and define λ as their average.

With no sum over Greek indices, integral length scales are defined by

$$L_{\alpha\alpha,\beta} = \frac{1}{\langle u_\alpha^2 \rangle} \int_0^{L_0/2} R_{\alpha\alpha}(r\boldsymbol{e}_\beta)\,\mathrm{d}r, \tag{6}$$

where $\boldsymbol{e}_\beta$ is the unit vector in the β-direction. The integration limit is taken to be $\frac{1}{2}L_0$ (instead of ∞ in the conventional definition) because the simulated flow (and hence $R_{ij}(\boldsymbol{r})$) is spatially periodic over a length L_0. For the turbulence not to be significantly affected by the period boundary condition, the correlation has to be small at separations of order $\frac{1}{2}L_0$. This condition is not closely met in these simulations (see §4.5, figure 35), but this is not of concern, since the large-scale motions are already affected by the forcing: we restrict our attention to the small scales.

Longitudinal (L_1) and transverse (L_2) integral lengthscales are defined by (6) with the choices $\alpha = \beta$ and $\alpha \neq \beta$, respectively, and averages are taken over statistically identical components. The eddy-turnover time T_e is based on the longitudinal integral scale, i.e. $T_e = L_1/u'$. In non-periodic homogeneous isotropic turbulence the lengthscale ratio L_1/L_2 is 2 (see e.g. Hinze 1975). The significant differences from this number evident in table 1 are due to periodicity and statistical error.

The three-dimensional energy spectrum function $E(k)$ (as defined in Tennekes & Lumley 1972) characterizes the radial distribution of energy in shells of radius k in wavenumber space. Its integral is the kinetic energy:

$$\tfrac{1}{2}q^2 = \int_0^{k_{\max}} E(k)\,\mathrm{d}k. \tag{7}$$

Rather than ∞, the upper integration limit is $k_{\max}$, the highest wavenumber treated. The small scales are well resolved only if the spectrum decays fast enough as this wavenumber is approached. The dissipation spectrum $D(k)$, defined by $2\nu k^2 E(k)$, similarly integrates to the volume-averaged dissipation $\langle\epsilon\rangle$. The numerical estimation of $E(k)$ and $D(k)$ is described by Eswaran & Pope (1988*b*).

The dissipation skewness (S_ϵ) is a high-order quantity sometimes used to characterize the small-scale behaviour (Kerr 1985): it is defined by

$$S_\epsilon = \frac{4}{35}\left(\frac{15\nu}{\langle\epsilon\rangle}\right)^{\frac{3}{2}} \int_0^{k_{\max}} \nu k^4 E(k)\,\mathrm{d}k. \tag{8}$$

Finally, we define another integral lengthscale Λ that is sometimes used (Monin & Yaglom 1975, p. 55), which is based on the energy spectrum:

$$\Lambda = \int_0^{k_{\max}} \frac{E(k)}{k}\,\mathrm{d}k. \tag{9}$$

Between the different simulations, Reynolds-number changes are effected by varying the size ratio between the energy-containing scales (dominated by forcing parameters) and the small scales (dominated by viscosity). The 128^3, $R_\lambda = 38$ and 63 simulations share the same forcing parameters: the increase in R_λ from 38 to 63 is achieved by lowering the viscosity, such that the small scales are reduced to a size just adequately resolved by the 128^3 grid ($k_{\max}\eta$ is 1.5). The 64^3, $R_\lambda = 38$ simulation has the same physical parameters as its 128^3 counterpart, but half the resolution ($k_{\max}\eta = 1.5$). Any differences (beyond statistical variability) between the results of these two $R_\lambda = 38$ simulations would reveal numerical error due to inadequate spatial resolution. That such differences are found to be small confirms that $k_{\max}\eta = 1.5$ represents adequate resolution.

To increase R_λ beyond 63, it is necessary to shift the energy towards the very lowest wavenumber band, while adjusting the viscosity to maintain the small-scale resolution. For the $R_\lambda = 90$ cases, only 18 wavenumber modes in a shell of radius $K_F = \sqrt{2}k_0$ are forced (and account for much of the energy), with T_F, ϵ^* and T_M^* unchanged. Because of the randomness inherent in the forcing scheme (and the turbulence itself), significant low-frequency temporal variations are observed in large-scale statistics (such as the volume-averaged kinetic energy and dissipation). This effect is much less pronounced for the $R_\lambda = 38$ and 63 cases, mainly because of the larger number of forced modes (92 compared to 18). The $R_\lambda = 90$ and 93 simulations are statistically identical, and the differences between the results affords a measure of the statistical variability. Two 64^3 simulations were performed with the same forcing parameters ($K_F = \sqrt{2}k_0$), but with a larger viscosity. The resulting Reynolds numbers are $R_\lambda = 54$ and 59 – the difference being entirely due to statistical variability. Further discussion on the effects of temporal variations of energy and dissipation is provided in the Appendix.

Owing to high CPU costs, the simulations were limited to less than six eddy-turnover times. However, this is sufficient time to obtain very large numbers of samples of small-scale quantities.

2.3. *Spectrum functions*

Here we present the Eulerian energy and dissipation spectrum functions to show that the small scales are well resolved, and appear similar to grid-generated turbulence. In figure 1,† the spectrum functions are shown for the 128^3, $R_\lambda = 38$ and 90 simulations, and also for 64^3, $R_\lambda = 38$. The plotting scales are chosen to emphasize the scale separation between energy-containing and dissipative eddies. The area under each curve is unity, when extended to zero wavenumber (note that $E(0)$ is zero since the mean velocity is zero). The peaks of the spectra represent (approximately) the wavenumber ranges contributing most to the energy dissipation. As is readily seen, the scale separation is relatively limited at $R_\lambda = 38$. At $R_\lambda = 90$, this separation is considerably wider, with the maximum of $E(k)$ occurring at k_0. However, logarithmic plots of $E(k)$ at this Reynolds number still do not show an extended 'five-thirds' region typical of an inertial subrange.

The accuracy of the 128^3, $R_\lambda = 38$ simulation is beyond reasonable doubt: $k_{max}\eta$ is 3.0. The close agreement between $D(k)$ for this simulation and for the 64^3, $R_\lambda = 38$ simulation indicates that the lesser resolution ($k_{max}\eta = 1.5$) is quite sufficient – at least for this statistic. The energy spectrum is less susceptible to errors arising from poor spatial resolution, but more susceptible to statistical errors: hence the small difference between the energy spectra for the two $R_\lambda = 38$ simulations.

The dissipation skewness S_ϵ (equation (7)), as a normalized fourth moment of the energy spectrum, provides an additional measure of small-scale accuracy. The $R_\lambda = 38$ and 63 simulations give values in the range 0.550 ± 0.025 and 0.516 ± 0.025 respectively. At comparable Reynolds numbers, Kerr (1985) found S_ϵ to be about 0.52 and 0.51, the dependence on R_λ being very weak. In fact, his data suggests that S_ϵ approaches 0.5 in the high-Reynolds-number limit. This appears to be qualitatively consistent with our results.

The closeness of the dissipation spectra for $R_\lambda = 38$ and 90 is remarkable, considering the large differences in the energy spectra. This suggests that the small

† In this and subsequent figures, symbols on solid lines are used merely for identification: their locations on these lines have no significance.

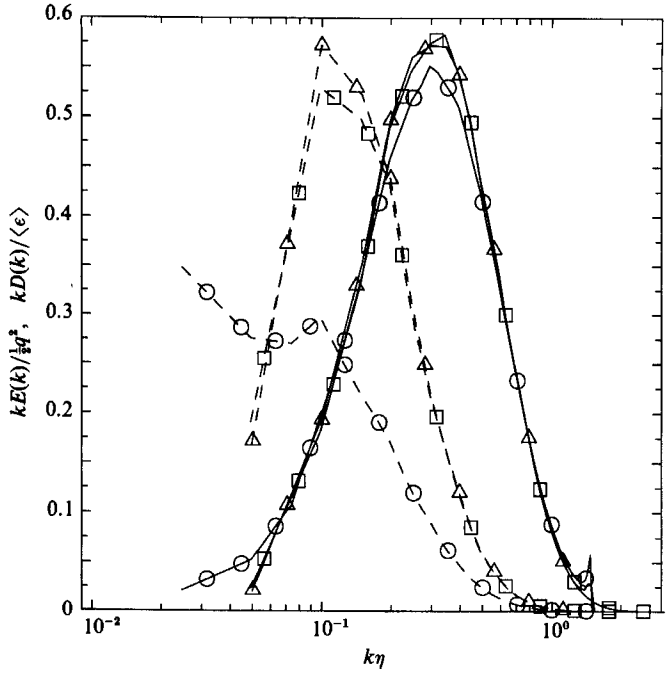

FIGURE 1. Normalized three-dimensional energy (dashed lines) and dissipation (solid lines) spectrum functions against Kolmogorov-scaled wavenumber. △, 64^3, $R_\lambda = 38$; □, 128^3, $R_\lambda = 38$; ○, 128^3, $R_\lambda = 90$. Curves start at k_0 and end at k_{max} for the respective grids.

scales are much less sensitive than the large scales to the numerical parameters of the forcing scheme.

To establish the physical relevance of the simulated small-scale structure, we compare the simulation spectra with those measured in grid-generated turbulence in wind-tunnel experiments. In figure 2, dashed lines represent data taken from the experiments of Comte-Bellot & Corrsin (1971), at a location where R_λ is 65. Good agreement between simulation and experiment is apparent at high wavenumbers. In contrast, the low-wavenumber spectra differ greatly, for several reasons. In the wavenumber range where it is active, the forcing scheme accounts for much of the observed bulge in the simulation (128^3, $R_\lambda = 63$) energy spectrum above the experimental data. In addition to forcing, the large eddies are affected by the periodic boundary conditions, since they are constrained to fit within the solution domain.

In figure 2, we also compare the 128^3, $R_\lambda = 63$ data (with $K_F = 2\sqrt{2}k_0$) with the 64^3 calculation at a similar Reynolds number ($R_\lambda = 59$, $K_F = \sqrt{2}k_0$). Although the spectra from different K_F necessarily differ for low wavenumbers, they agree well for both intermediate and high wavenumbers. Thus, in accordance with the more thorough examination of Eswaran & Pope (1988*a*), we conclude that the forcing has little effect on the small scales.

To summarize, we have confirmed our expectations that artificial forcing and periodic boundary conditions have distorting influences on the large scales, but the small scales are not appreciably affected. The small scales of the flow field are accurately simulated (with $k_{max}\eta \approx 1.5$ or greater), and are found to be representative of turbulence observed in the laboratory. This justifies the present study of small-scale statistics.

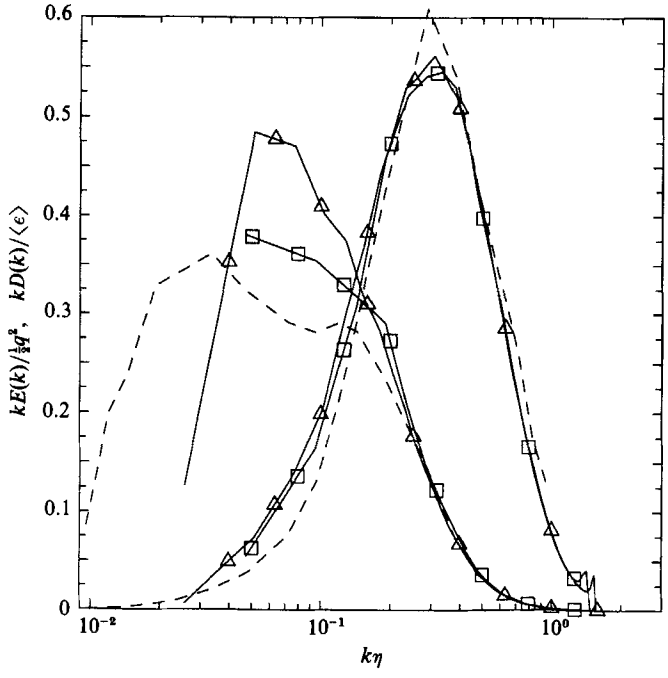

FIGURE 2. Normalized three-dimensional energy and dissipation spectrum functions against Kolmogorov-scaled wavenumber. △, 128^3, $R_\lambda = 63$; □, 64^3, $R_\lambda = 59$; dashed lines, experimental data from Comte-Bellot & Corrsin (1971), $R_\lambda = 65$.

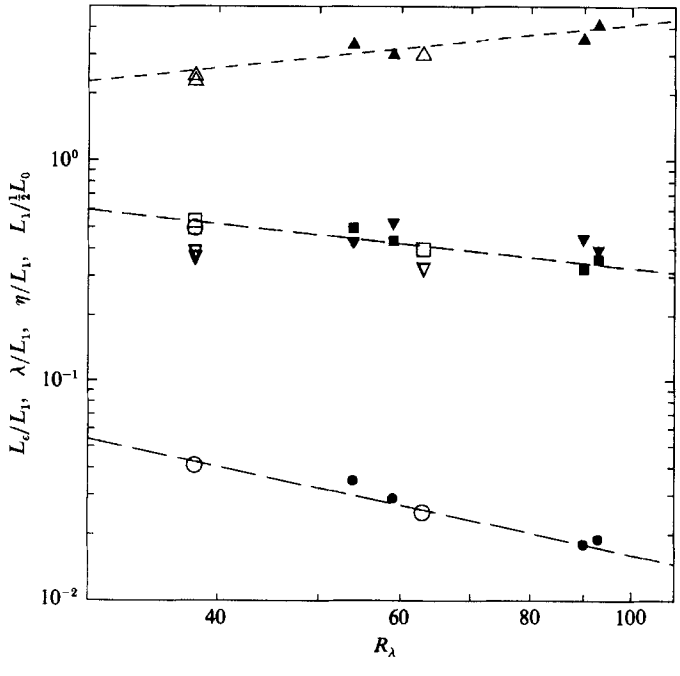

FIGURE 3. Ratios of Eulerian lengthscales against Reynolds number, for the simulations listed in table 1. Open symbols for $K_F/k_0 = 2\sqrt{2}$, solid symbols for $K_F/k_0 = \sqrt{2}$. △, L_e/L_1; □, λ/L_1; ○, η/L_1; ▽, $L_1/\frac{1}{2}L_0$. Dashed lines indicate approximate Reynolds-number dependence of the data: logarithmic slopes $\frac{1}{2}$, $-\frac{1}{2}$ and -1.

2.4. *Eulerian scales*

Figure 3 is a log–log plot of different normalized lengthscales against R_λ. As expected, the simulations with $K_F = \sqrt{2}k_0$ (solid symbols) yield slightly greater values of the integral lengthscale $L_1/(\frac{1}{2}L_0)$ than do the simulations with $K_F = 2\sqrt{2}k_0$ (open symbols). But a clear dependence of $L_1/(\frac{1}{2}L_0)$ on R_λ is not evident. The other ratios shown do vary with R_λ, but appear to be insensitive to K_F/k_0.

It may be seen that the dissipation lengthscale ($L_\epsilon \equiv (\frac{1}{2}q^2)^{\frac{3}{2}}/\langle\epsilon\rangle$) increases (compared to L_1) approximately as the square-root of R_λ. This implies that the the conventional high-Reynolds-number scaling ($\langle\epsilon\rangle \sim u'^3/L_1$) is not precisely followed. From the definitions of L_ϵ, λ and η it follows that λ/L_ϵ and η/L_ϵ vary as R_λ^{-1} and $R_\lambda^{-\frac{3}{2}}$ respectively. But because L_ϵ/L_1 increases as $R_\lambda^{\frac{1}{2}}$, inevitably λ/L_1 and η/L_1 decrease more slowly (approximately as $R_\lambda^{-\frac{1}{2}}$ and R_λ^{-1} respectively).

3. Extraction and analysis of Lagrangian data

3.1. *Particle-tracking algorithm*

Yeung & Pope (1988) studied in detail the numerical problem of tracking fluid particles, and described and tested an accurate scheme. Here we give only the essential details.

Let $\boldsymbol{x}^+(\boldsymbol{y}, t)$ and $\boldsymbol{u}^+(\boldsymbol{y}, t)$ denote† the position and velocity at time t of the fluid particle originating from position $\boldsymbol{y}$ at time $t = 0$. Each particle is tracked by numerically integrating its equation of motion, which is simply

$$\frac{\partial \boldsymbol{x}^+(\boldsymbol{y}, t)}{\partial t} = \boldsymbol{u}^+(\boldsymbol{y}, t). \tag{10}$$

The Lagrangian velocity $\boldsymbol{u}^+(\boldsymbol{y}, t)$ is related to the Eulerian velocity $\boldsymbol{u}(\boldsymbol{x}, t)$ by

$$\boldsymbol{u}^+(\boldsymbol{y}, t) = \boldsymbol{u}(\boldsymbol{x}^+(\boldsymbol{y}, t), t). \tag{11}$$

A second-order Runge–Kutta method is used to calculate particle displacements. Let t_n and t_{n+1} be successive time levels ($t_{n+1} = t_n + \Delta t$). Given the current position $\boldsymbol{x}^+(t_n)$, the predictor step yields an estimate $\boldsymbol{x}^*$ of the future position $\boldsymbol{x}^+(t_{n+1})$:

$$\boldsymbol{x}^* = \boldsymbol{x}^+(t_n) + \Delta t\, \boldsymbol{u}^+(t_n). \tag{12}$$

The corrector step then gives the improved approximation:

$$\boldsymbol{x}^+(t_{n+1}) = \boldsymbol{x}^+(t_n) + \tfrac{1}{2}\Delta t\,[\boldsymbol{u}^+(t_n) + \boldsymbol{u}(\boldsymbol{x}^*, t_{n+1})]. \tag{13}$$

Interpolation is needed to determine the fluid particle velocity $\boldsymbol{u}^+(t_n)$ (and also $\boldsymbol{u}(\boldsymbol{x}^*, t_{n+1})$) from the Eulerian velocity field $\boldsymbol{u}(\boldsymbol{x}, t)$ which is known at the N^3 grid nodes in physical space. This interpolation is the dominant source of numerical error in the extraction of Lagrangian data. The interpolation error mainly depends on the spatial resolution of the small-scale motions (requiring $k_{\max}\eta$ to be at least 1.0) and the interpolation scheme used. Two accurate interpolation schemes have been evaluated (Yeung & Pope 1988): a third-order, thirteen-point, Taylor-series scheme; and fourth-order cubic splines. Besides having superior accuracy, cubic splines have the advantage of yielding twice-continuously differentiable approximations to the interpolated variables. This leads to a low level of numerical noise in the time series

† A superscript $^+$ denotes Lagrangian quantities (i.e. those following a fluid particle). We also abbreviate the notation to $\boldsymbol{x}^+(t)$, $\boldsymbol{u}^+(t)$, etc. where appropriate.

obtained. Cubic splines are used here (whereas Yeung & Pope 1987 used the Taylor-series scheme).

In homogeneous turbulence, all fluid particles having different initial positions are statistically identical. Ensemble averages can thus be taken over all (M) particles used. In the 128^3 simulations, we choose the initial locations to be coincident with a subset of 4096 (i.e. 16^3) Eulerian grid points, which form an equispaced cubic sublattice. This choice has the advantage of achieving close to maximum statistical independence between the particles and hence minimum sampling errors for a given value of M. However, for the 64^3 simulations we used only 1600 particles, and initialized the locations by taking samples from a uniform random-number generator. No gross effect of sampling errors is apparent.

3.2. *Velocity gradient invariants*

Velocity-gradient information is also extracted from the simulations and presented. As in (11), the Lagrangian time series of any variable θ (such as a component of $\partial u_i/\partial x_j$) can be obtained from the Eulerian field $\theta(\boldsymbol{x}, t)$ by

$$\theta^+(\boldsymbol{y}, t) = \theta(\boldsymbol{x}^+(\boldsymbol{y}, t), t). \tag{14}$$

The Eulerian velocity-gradient fields can be generated with high accuracy by performing the differentiation in wavenumber space. It is thus possible to obtain the time series of Lagrangian velocity gradients† $(\partial u_i/\partial x_j)^+$. However, this direct method is computationally expensive: for each component of velocity gradient, it requires a discrete Fourier transform (to obtain $\partial u_i/\partial x_j$ in physical space), and then the fitting of a cubic spline. An inexpensive alternative is to obtain the gradients by differentiating the cubic spline fitted to the velocity field. The loss of accuracy is insubstantial for well-resolved Eulerian fields. With this procedure, the Lagrangian velocity gradients do not identically satisfy the continuity equation $(\partial u_i/\partial x_i)^+ = 0$. A correction – albeit small – is therefore applied to the data: the corrected gradients are

$$\left(\frac{\partial u_i}{\partial x_j}\right)^+ = \left(\frac{\partial \tilde{u}_i}{\partial x_j}\right)^+ - \frac{1}{3}\left(\frac{\partial \tilde{u}_l}{\partial x_l}\right)^+ \delta_{ij}, \tag{15}$$

where the tilde refers to the raw data before correction.

The Lagrangian strain rates s_{ij}^+ and rotation rates r_{ij}^+ are then readily evaluated, as the symmetric and antisymmetric parts of $(\partial u_i/\partial x_j)^+$.

According to the turbulent kinetic energy equation, the (mechanical) dissipation rate following a fluid particle, $\epsilon^+(t)$, is given by‡

$$\epsilon^+(t) = 2\nu s_{ij}^+ s_{ij}^+. \tag{16}$$

Since $\epsilon^+(t)$ is quadratic in the velocity gradients, which exhibit much greater local variation than the velocities, better resolution is required for accuracy. The data of Yeung & Pope (1988) shows that for $k_{\max}\eta \approx 1.5$, cubic spline interpolation gives about 1% error in the velocity gradients (compared to 0.3% for velocities).

As may be seen in (16), the dissipation rate is proportional to the second invariant

† Note that $(\partial u_i/\partial x_j)^+$ is the derivative of the Eulerian velocity field, evaluated at the fluid particle location: it is different from $\partial u_i^+/\partial y_j^+$, the derivative with respect to the Lagrangian coordinates.

‡ The quantity $\varphi^+(t)$ defined by (18) was inappropriately referred to as the dissipation in Yeung & Pope (1987).

('squared magnitude') of the strain rate. We also study the analogous quantities formed from rotation rate and velocity gradients, namely

$$\zeta^+(t) = 2\nu r_{ij}^+ r_{ij}^+, \tag{17}$$

and

$$\varphi^+(t) = \nu\left(\frac{\partial u_i}{\partial x_j}\right)^+\left(\frac{\partial u_i}{\partial x_j}\right)^+. \tag{18}$$

We (loosely) refer to $\zeta^+(t)$ as the 'enstrophy' since it is a measure of vorticity ($\boldsymbol{\omega}$) squared:

$$r_{ij}\, r_{ij} = \tfrac{1}{2}\omega_k\, \omega_k. \tag{19}$$

For want of a better expression, we refer to $\varphi^+(t)$ as the 'pseudo-dissipation'.

These three velocity-gradient invariants, $\epsilon^+(t)$, $\zeta^+(t)$ and $\varphi^+(t)$, are related by

$$\varphi^+(t) = \tfrac{1}{2}[\epsilon^+(t) + \zeta^+(t)]. \tag{20}$$

In homogeneous turbulence, the Lagrangian and Eulerian (one-point, one-time) probability densities are identical. It follows readily that the three invariants are equal *in expectation*† i.e.

$$\langle\epsilon\rangle = \langle\epsilon^+(t)\rangle = \langle\varphi^+(t)\rangle = \langle\zeta^+(t)\rangle. \tag{21}$$

Although $\epsilon^+(t)$, $\zeta^+(t)$ and $\varphi^+(t)$ share the same mean value, other statistical characteristics are found to be quite different.

3.2. *Statistical analysis*

We now give a brief account of the statistical processing procedures used. During the simulations, at regular time intervals h (an integer multiple of Δt), the Lagrangian data $\boldsymbol{u}^+(t)$, $(\partial u_i/\partial x_j)^+(t)$ (from which $\zeta^+(t)$ and $\varphi^+(t)$ are readily calculated) and $\epsilon^+(t)$ are stored for subsequent analysis. To resolve temporal variations of all frequencies, the sampling interval h needs to be small compared with the Kolmogorov timescale (τ_η): for the present purposes, $h/\tau_\eta \approx 1/8$ is found to be adequate. Since the Eulerian velocity fields are stationary and homogeneous, the Lagrangian variables are stationary random functions of time. Standard time-series analyses are performed on the data.

Autocorrelations are calculated for three purposes: for presentation; to estimate integral timescales; and to form spectra by Fourier transformation. For the first two purposes we use the standard unbiased estimator (see e.g. Priestley 1981, §5.3.3) to calculate the autocovariance, and then normalize to obtain the autocorrelation. However, this unbiased estimate is known to be not necessarily positive semidefinite, and can lead to energy spectra with negative spectral values. Thus, to evaluate frequency spectra we follow standard practice and use a biased positive semidefinite estimator (also described in the same section of Priestley 1981). Two-time cross-correlation functions are estimated in the same (unbiased) manner as for single-variable autocorrelations. For two stationary processes X and Y, this function is the correlation coefficient between $X(t)$ and $Y(t+\tau)$, denoted by $\rho(X, Y; \tau)$ (independent of t). (We use ρ as a general symbol for one- or two-time, auto- or cross-correlations. The meaning is always clear in context.)

A correction procedure for numerical noise is necessary for the high-frequency part of the spectra. It is modelled after that used by Mestayer (1982) and is described by Yeung & Pope (1988).

† When used on Lagrangian variables, angled brackets denote ensemble averages which are estimated by taking the mean over all particles, over all sampled time levels and over all statistically identical components.

The Lagrangian velocity increment over a time interval τ is denoted by

$$\Delta_\tau u^+(t) = u^+(t+\tau) - u^+(t). \tag{22}$$

(u or u^+ (without subscripts) refers to any component of $\boldsymbol{u}$, or, in the case of mean values, to averages over all components.) The mth order moment of $\Delta_\tau u^+(t)$ is, by definition, the mth order Lagrangian velocity structure function, $D_m^{\mathrm{L}}(\tau)$. These structure functions are used to study the non-Gaussianity of the velocity increments, often by comparing the flatness factor $\mu_4(\tau) \equiv D_4^{\mathrm{L}}(\tau)/D_2^{\mathrm{L}}(\tau)^2$ and superskewness $\mu_6(\tau) \equiv D_6^{\mathrm{L}}(\tau)/D_2^{\mathrm{L}}(\tau)^3$ with the Gaussian values (3 and 15).

With a sufficiently fast sampling rate (small enough h), the fluid particle acceleration $\boldsymbol{a}^+$ can be approximated by a simple central difference in terms of the velocity increment: $\boldsymbol{a}^+(t+\frac{1}{2}h)$ is equated to $(1/h)\ \Delta_h \boldsymbol{u}^+(t)$. We also study the acceleration magnitude $|\boldsymbol{a}^+|$ ($\equiv (\boldsymbol{a}^+ \cdot \boldsymbol{a}^+)^{\frac{1}{2}}$).

Following Tennekes (1975), the Lagrangian time microscale τ_{L} is defined by

$$\tau_{\mathrm{L}} = \left[\frac{2\langle u^{+2}\rangle}{\langle (\mathrm{d}u^+/\mathrm{d}t)^2\rangle}\right]^{\frac{1}{2}}, \tag{23}$$

taking component averages. Since it is directly related to the curvature of the Lagrangian velocity autocorrelation $\rho_{\mathrm{L}}(\tau)$ at the origin (see e.g. Tennekes & Lumley 1972), the microscale is important when autocorrelations at small time lag are examined. Although the microscale can theoretically be determined from the autocorrelations near the origin, it is found to be highly sensitive to even small numerical errors in these autocorrelations. Instead, we use (23) for the determination of the microscale.

4. Results

In this section, we focus on the physical significance of the Lagrangian and Eulerian time statistics obtained from the 128^3 simulations at $R_\lambda = 38, 63, 90$ and 93, especially concerning the intermittent behaviour of the small scales. Selected data from 64^3 calculations are also included.

In successive subsections, we discuss: (1) Reynolds-number dependence of acceleration statistics in regular and locally stretched time frames; (2) Lagrangian velocity autocorrelations and frequency spectra; (3) velocity increment statistics, and their applications for stochastic models of fluid-particle velocity; (4) statistics of acceleration magnitude, dissipation, enstrophy and pseudo-dissipation; and (5) statistics of the Eulerian time velocity and its time derivative.

4.1. *Reynolds-number dependence of acceleration*

According to the Kolmogorov (1941) hypotheses, at high Reynolds numbers, small-scale statistics scaled by the Kolmogorov scales are universal. We have already observed (figure 1) that the Eulerian dissipation spectra appear universal, even at the lowest Reynolds number simulated. Other Eulerian statistics (e.g. the skewness of $\partial u_1/\partial x_1$) exhibit a weak Reynolds-number dependence that is generally attributed to internal intermittency (Monin & Yaglom 1975), and accounted for by Kolmogorov's (1962) refined hypotheses.

To examine the question of Reynolds-number dependence of Lagrangian statistics, we focus on the moments and autocorrelation of the acceleration. According to

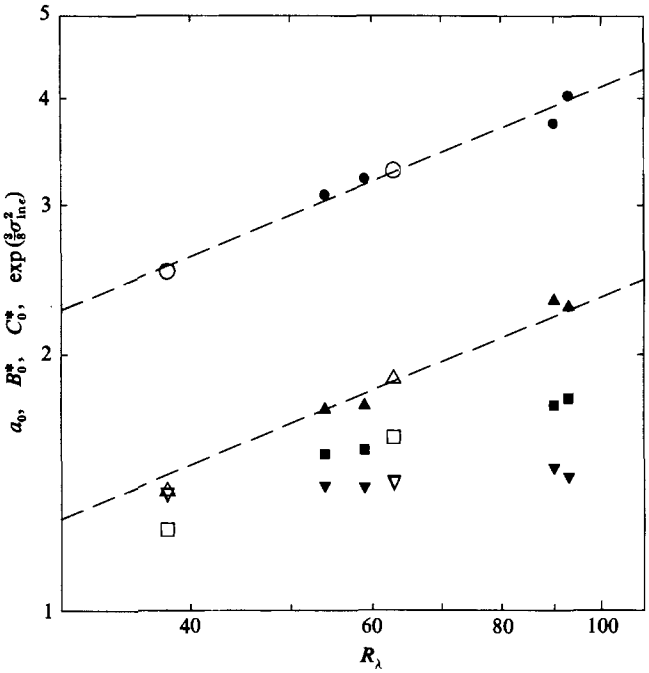

FIGURE 4. Values of the normalized quantities a_0, B_0^*, C_0^*, etc., defined in §§4.1–4.3 against R_λ, for the 128^3 and two 64^3 ($R_\lambda = 54, 59$) simulations. Open symbols for $K_F/k_0 = 2\sqrt{2}$, solid symbols for $K_F/k_0 = \sqrt{2}$. △, a_0; □, B_0^*; ○, C_0^*; ▽, $\exp(\frac{3}{8}\sigma^2_{\ln\epsilon})$. Dashed lines of logarithmic slopes $\frac{1}{2}$ indicate approximate Reynolds-number dependence of a_0 and C_0^*.

Kolmogorov's (1941) hypotheses, the acceleration variance $\langle a^{+2}\rangle$ ($\equiv \frac{1}{3}\langle \boldsymbol{a}^+ \cdot \boldsymbol{a}^+\rangle$) is given by

$$\langle a^{+2}\rangle = a_0 \frac{v_\eta^2}{\tau_\eta^2} = a_0 \langle\epsilon\rangle^{\frac{3}{2}}/\nu^{\frac{1}{2}}, \tag{24}$$

where a_0 is a universal constant. The values of a_0 obtained from each simulation (from (24)) are plotted against R_λ in figure 4. It may be seen that there is a strong Reynolds-number dependence (approximately $a_0 \sim R_\lambda^{\frac{1}{2}}$).

It is natural to investigate whether the Reynolds-number dependence can be explained by Kolmogorov's refined hypotheses. The standard application of these hypotheses (Monin & Yaglom 1975) is to replace $\langle\epsilon\rangle^{\frac{3}{2}} = \langle\epsilon^+\rangle^{\frac{3}{2}}$ by $\langle\epsilon^{+\frac{3}{2}}\rangle$ in (24), and to assume that $\ln\epsilon^+$ is normally distributed (with variance denoted by $\sigma^2_{\ln\epsilon}$). Then, in place of (24) we obtain

$$a_0 \equiv \frac{\langle a^{+2}\rangle}{(v_\eta/\tau_\eta)^2} = \overline{a_0}\frac{\langle\epsilon^{+\frac{3}{2}}\rangle}{\langle\epsilon\rangle^{\frac{3}{2}}} = \overline{a_0}\exp(\tfrac{3}{8}\sigma^2_{\ln\epsilon}), \tag{25}$$

where $\overline{a_0}$ is a universal constant. We find (§4.4) that $\ln\epsilon^+$ is, indeed, approximately normally distributed, and values of $\sigma^2_{\ln\epsilon}$ are given in table 4. Using these values, and taking $\overline{a_0} = 1$, the predicted values of a_0 are shown in figure 4. It may be seen that the Reynolds-number dependence predicted by (25) is much weaker than observed.

While (25) is unsuccessful in explaining the observed Reynolds-number dependence of $\langle a^{+2}\rangle$, it may be that a different scaling is successful. We consider scalings based on either dissipation or pseudo-dissipation. Let ϕ^+ denote either ϵ^+ or φ^+, and let q

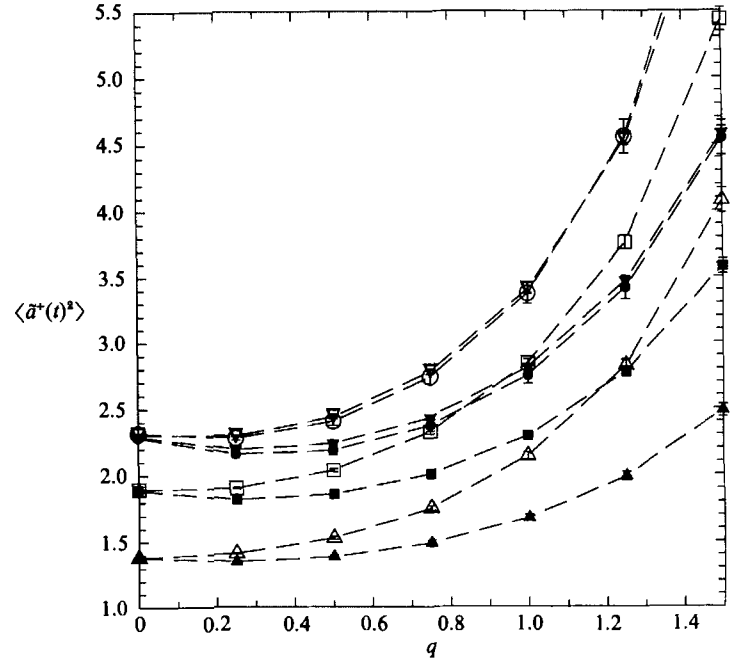

FIGURE 5. Variance of locally scaled acceleration components (equation (26)) against the scaling exponent (q), for the 128^3 simulations. Open symbols for scaling by dissipation (ϵ^+), solid symbols for scaling by pseudo-dissipation (φ^+): △, $R_\lambda = 38$; □, $R_\lambda = 63$; ○, $R_\lambda = 90$; ▽, $R_\lambda = 93$. Data higher than the plot limits are not shown.

be a parameter to be chosen. We define the normalized acceleration under generalized local scaling by

$$\tilde{\boldsymbol{a}}^+(t) = \frac{\boldsymbol{a}^+(t)}{\{v_\eta/\tau_\eta\}} \left[\frac{\phi^+(t)}{\langle \phi \rangle}\right]^{-q/2}. \tag{26}$$

Here the curly braces indicate global mean values, i.e. $\{v_\eta/\tau_\eta\} \equiv (\langle \epsilon \rangle^3/\nu)^{\frac{1}{4}}$. Both $\boldsymbol{a}^+(t)$ and $\phi^+(t)$ are preprocessed as described in the Appendix. (The calculated mean values of the chosen ϕ^+, i.e. $\langle \epsilon^+ \rangle$ or $\langle \varphi^+ \rangle$, are, of course, nearly equal.) We seek a scaling (i.e. a choice of ϕ^+ and q) that makes the statistics of $\tilde{\boldsymbol{a}}^+(t)$ independent of Reynolds number (or nearly so). The scaling implied by the Kolmogorov (1941) hypotheses is $q = 0$, while for the refined 1962 hypotheses it is $\phi^+ = \epsilon^+$, $q = \frac{3}{2}$.

Figure 5 shows the variances of the locally scaled acceleration components $\tilde{a}^+(t)$ from the four 128^3 simulations. Evidently, no combination of q and ϕ^+ (including the choice implied by the refined Kolmogorov hypotheses) results in universality, at least in the Reynolds-number range of the simulations. The error bars (barely visible at most points) show the standard errors which are estimated by dividing the time series into subrecords and processing each separately. Their limited extent indicates that these findings are well beyond the range of statistical uncertainty.

Figure 6 shows the flatness factors of $\tilde{a}^+(t)$ under the same conditions. It may be seen that without local scaling (i.e. $q = 0$) the flatness factor increases with R_λ, consistent with the notion of internal intermittency. The flatness factors are extremely high for the larger values of q under dissipation scaling. Such high values are deemed to be not accurate, in view of the large statistical errors that are evident. On the other hand, scaling by pseudo-dissipation leads to relatively low flatness

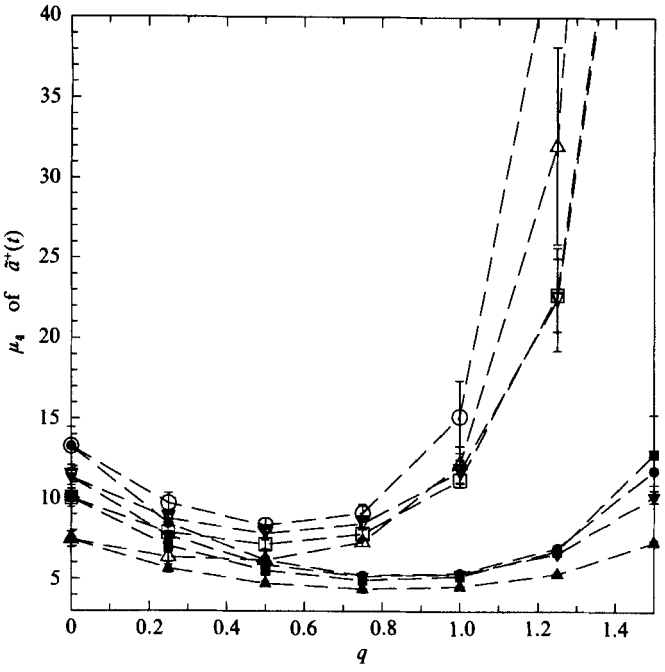

FIGURE 6. Flatness factor of locally scaled acceleration components against scaling exponents. Symbols same as in figure 5.

factors. A minimum between 4.5 and 6.0 is attained at around $q = \frac{3}{4}$ or 1, where the Reynolds-number dependence is also relatively weak.

In summary, the acceleration variance (normalized by the Kolmogorov scales) is found to increase (approximately) as the square-root of R_λ. Neither Kolmogorov's (1962) refined hypotheses, nor a more general local scaling (equation (26)) is capable of accounting for this strong Reynolds-number dependence. It is found, however, that the local scaling with $\phi^+ = \varphi^+$ and $q = 1$ yields fairly small flatness factors of acceleration, virtually independent of R_λ: the significance of this result is discussed in §4.3.

We now examine the autocorrelation function of acceleration, $\rho_a(\tau)$. Since this is a normalized quantity ($\rho_a(0) = 1$), it is possible for it to be independent of Reynolds number even though the acceleration variance is not. Figure 7 shows the 128^3 simulation data, against Kolmogorov-scaled time lag. The autocorrelation functions have the form typical for the derivative of a stationary process with finite non-zero integral scale (in this case, $\boldsymbol{u}^+(t)$): their values are negative at long time lags, and the acceleration integral timescales are practically zero (Tennekes & Lumley 1972).

The zero-crossing time τ_a (defined such that $\rho_a(\tau_a) = 0$) varies little with R_λ when normalized by τ_η: for all of the simulations τ_a/τ_η is within 2% of 2.2. On the other hand, the minimum of $\rho_a(\tau)$ shows significant systematic variations.

A local scaling of both acceleration and time is sought to achieve a substantial reduction of Reynolds-number dependence of the acceleration autocorrelation function. We define a new time variable $\hat{t}$:

$$\mathrm{d}\hat{t} = \mathrm{d}t\left[\frac{\phi^+(t)}{\langle\phi\rangle}\right]^m. \tag{27}$$

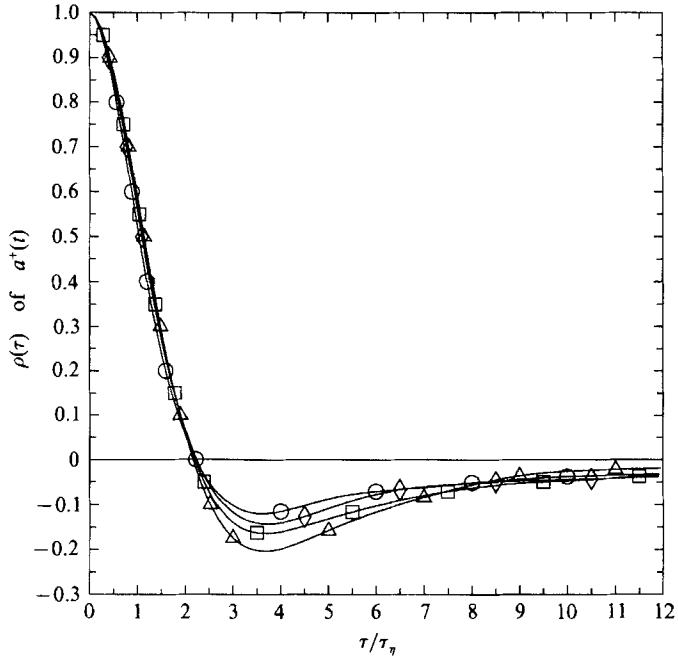

FIGURE 7. Autocorrelation functions of acceleration components against time lag normalized by the Kolmogorov scale from the 128^3 simulations. The autocorrelations are nearly zero for time lags beyond the range shown. △, $R_\lambda = 38$; □, $R_\lambda = 63$; ○, $R_\lambda = 90$, ◇, $R_\lambda = 93$.

We refer to t and $\hat{t}$ as regular time and stretched time, respectively. A natural choice of m is $\frac{1}{2}$: it is equivalent to scaling by a 'local' Kolmogorov timescale following a fluid particle. In addition, use of $q = \frac{3}{4}$, $\phi^+ = \varphi^+$ is strongly suggested by the flatness factor data as noted above. The autocorrelations of $\tilde{a}(\hat{t})$ (which is derived from $\tilde{a}^+(t)$ by transforming to the stretched time axis $\hat{t}$) are shown in figure 8. It may be seen that, with these choices of m, q and ϕ^+, a good collapse of the data is obtained. However, this is achieved only by normalizing the time lag τ (in stretched time) by the zero-crossing time $\tilde{\tau}_a$. The ratio $\tilde{\tau}_a/\tau_\eta$ has 10% variations around the value 2.5 – the variations being at least partly statistical (note the values for $R_\lambda = 90$ and 93). Detailed tests reveal that stretching the time by $m = \frac{1}{2}$ in (27) is the most important factor contributing to the observed near-universality.

Unlike the unscaled acceleration component $a^+(t)$, neither of the scaled versions, $\tilde{a}^+(t)$ and $\tilde{a}^+(\hat{t})$, represents the derivative of a stationary process. Thus, they do not possess the zero-integral-scale property. However, the integral scales are found to be small, and do not affect the autocorrelation curve at the short time lags of interest.

The goal of this subsection has been to discover a local scaling which would achieve near-universality in acceleration statistics, by taking into account the role of intermittency (through the dissipation or pseudo-dissipation fluctuations). Partial success has been possible only for the flatness factors and autocorrelations, using scaling based on pseudo-dissipation with suitable exponents (m and q) as found above. The Reynolds-number dependence displayed by the unscaled acceleration statistics is attributed to the increase of intermittency with Reynolds number; but the dependence is much stronger than that predicted by the refined Kolmogorov (1962) hypotheses. While the Reynolds numbers of our simulations are too low for these hypotheses to be applied convincingly, it should nevertheless be recognized

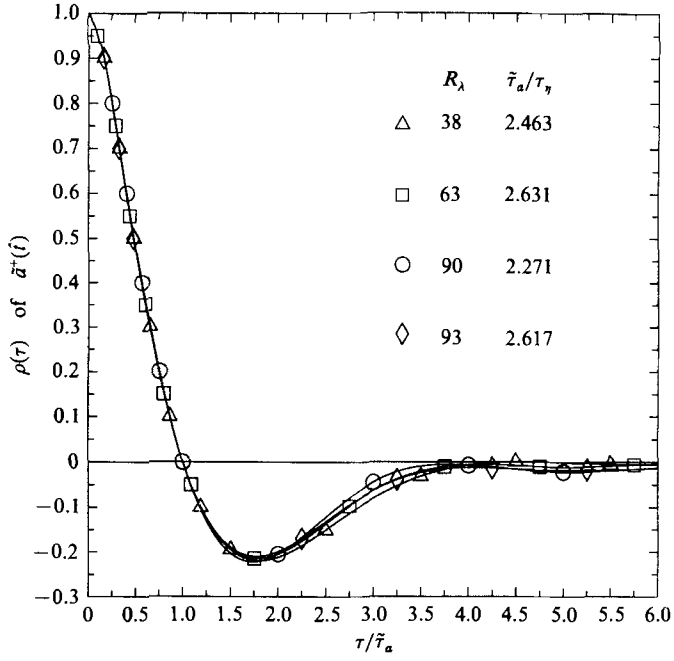

FIGURE 8. Autocorrelation functions of acceleration components for same simulations as in figure 7, but in stetched time $\hat{t}$ based on local pseudo-dissipation φ^+ and exponents $q = \frac{3}{4}$, $m = \frac{1}{2}$. Time lag is normalized by the zero-crossing time $\tilde{\tau}_a$, the ratios $\tilde{\tau}_a/\tau_\eta$ being as indicated.

that many Eulerian statistics (e.g. the Kolmogorov-scaled dissipation spectrum and dissipation skewness) show little variation of the Reynolds-number range considered here.

The data presented in the subsections to follow support the conclusions that Lagrangian statistics display strong Reynolds-number dependence, and for the purpose of reducing this dependence through local scaling (on which stochastic models may be based), the statistical properties of the pseudo-dissipation φ^+ are more favourable than those of the dissipation ϵ^+.

4.2. *Autocorrelations and frequency spectra*

In this subsection we present the Lagrangian velocity autocorrelations and velocity and acceleration frequency spectra. Numerical data are summarized in table 2.

The Lagrangian velocity autocorrelation, $\rho_L(\tau)$, important for turbulent diffusion studies, has been obtained in some experiments (Snyder & Lumley 1971; Shlien & Corrsin 1974; Sato & Yamamoto 1987). Figure 9 shows the simulation results, with time lag normalized by the Lagrangian integral timescale T_L. Near the origin, the $R_\lambda = 38$ curve drops off more slowly than the others. This reflects the fact (see table 2) that the ratio of microscale to integral scale, i.e. τ_L/T_L, decreases with Reynolds number.

For small time lags, the calculated autocorrelations fall off more slowly than do the data from the decaying turbulence experiments of Sato & Yamamoto. Several of their data points are also shown in figure 9. The exponential function, i.e. $\exp(-\tau/T_L)$, agrees well with both simulation and experiment beyond one integral timescale, even though its behaviour near the origin is qualitatively incorrect (its microscale is undefined). It may be observed from table 2 that T_L/T_e – the ratio of the

	$R_\lambda = 38$	$R_\lambda = 38$	$R_\lambda = 54$	$R_\lambda = 59$	$R_\lambda = 63$	$R_\lambda = 90$	$R_\lambda = 93$
N	64	128	64	64	128	128	128
K_F/k_0	$2\sqrt{2}$	$2\sqrt{2}$	$\sqrt{2}$	$\sqrt{2}$	$2\sqrt{2}$	$\sqrt{2}$	$\sqrt{2}$
$h/\Delta t$	8	10	4	4	6	4	4
τ_η/h	5.00	8.62	5.97	5.95	6.97	9.16	8.56
$\dfrac{\langle a^{+2}\rangle}{v_\eta^2/\tau_\eta^2}$	1.24	1.38	1.72	1.74	1.87	2.32	2.28
T/T_L	12.9	8.07	12.5	11.7	8.18	7.64	8.39
T_L/τ_c	0.377	0.352	0.288	0.290	0.291	0.247	0.231
T_L/τ_η	5.45	5.15	6.03	6.46	7.02	8.57	8.36
T_L/T_e'	0.74	0.66	0.78	0.71	0.71	0.72	0.78
τ_L/T_L	0.72	0.73	0.67	0.64	0.59	0.52	0.55
μ_4 of $\Delta_h u^+$	7.6	8.0	10.1	8.1	11.1	17.8	11.7

TABLE 2. Velocity, acceleration and velocity increments

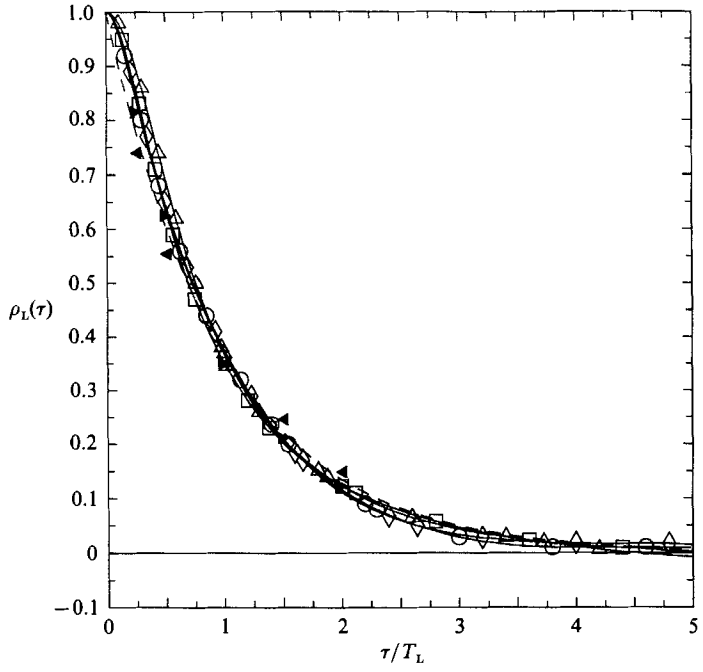

FIGURE 9. Lagrangian velocity autocorrelation functions $\rho_L(\tau)$ against time lag normalized by the Lagrangian integral timescale T_L, from the 128^3 simulations. △, $R_\lambda = 38$; □, $R_\lambda = 63$; ○, $R_\lambda = 90$; ◇, $R_\lambda = 93$. The dashed line is the function $\exp(-\tau/T_L)$. Experimental data from Sato & Yamamoto (1987): ▶, $R_\lambda = 46$; ◀, $R_\lambda = 66$.

Lagrangian integral timescale to the eddy-turnover time – is about 0.72 ± 0.06: a systematic variation with R_λ is not evident. This ratio is quite plausibly flow-dependent: measurements suggest it to be ≈ 1.0 in grid turbulence (Shlien & Corrsin 1974), but ≈ 1.7 in the near-ground convective boundary layer (Hanna 1981).

In the context of turbulent dispersion, the significance of the Lagrangian velocity autocorrelation is that it determines the root-mean-square (r.m.s.) displacement of fluid particles (Taylor 1921). Let s be the time t normalized by the Lagrangian integral timescale T_L, and let $\Sigma(s)$ be the r.m.s. displacement of a fluid particle

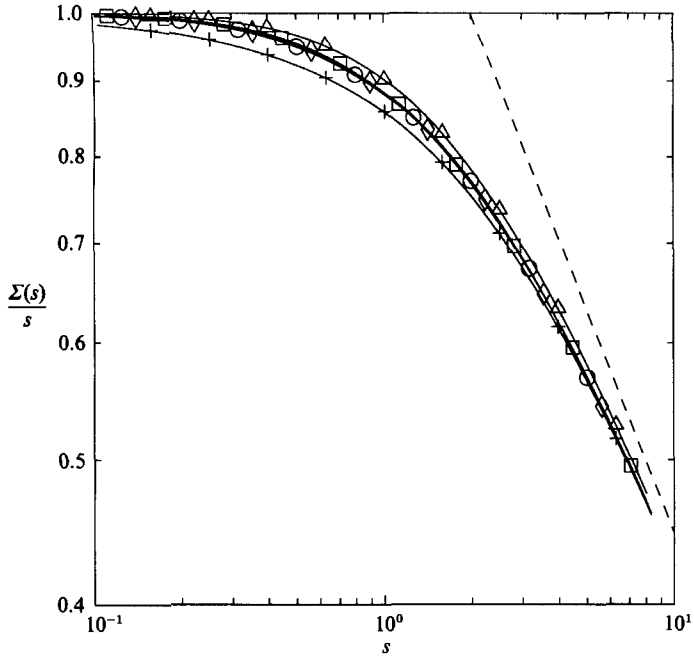

FIGURE 10. Normalized r.m.s. particle displacement $\Sigma(s)$, plotted as $\Sigma(s)/s$ against the normalized time $s(\equiv t/T_{\mathrm{L}})$, for the 128^3 simulations. △, $R_\lambda = 38$; □, $R_\lambda = 63$; ○, $R_\lambda = 90$; ◇, $R_\lambda = 93$; +, exponential autocorrelation: $\rho_{\mathrm{L}}(\tau) = \exp(-\tau/T_{\mathrm{L}})$. Small-time asymptote $\Sigma(s) = s$ is the upper x-axis; large-time asymptote $\Sigma(s) = (2s)^{\frac{1}{2}}$ is the dashed line.

(relative to its position at $t = 0$) normalized by $u'T_{\mathrm{L}}$. Then from the standard dispersion relations (e.g. Hinze 1975, p. 53) for stationary isotropic turbulence we obtain

$$\Sigma(s)^2 = 2\int_0^s \rho_{\mathrm{L}}(s')\,(s-s')\,\mathrm{d}s'. \tag{28}$$

Figure 10 shows $\Sigma(s)/s$ plotted against s for the 128^3 simulations, and according to the exponential approximation to the autocorrelation. Plotting $\Sigma(s)/s$ rather than $\Sigma(s)$ accentuates the slight differences between the curves. Only the lowest Reynolds-number case is perceptibly different from the others. The slight difference between $\Sigma(s)$ according to the exponential autocorrelation and those obtained from the simulations is due to the qualitative differences in the autocorrelations at small times. The small-time asymptote $\Sigma(s) = s$, and the large-time asymptote $\Sigma(s) = (2s)^{\frac{1}{2}}$ (deduced from (28)) are also shown on the figure. The principal conclusion is that the dispersion is mainly determined by u' and T_{L}: the effect of Reynolds number on $\rho_{\mathrm{L}}(\tau)$ is too weak to affect $\Sigma(s)$ appreciably.

It is emphasized that the velocity autocorrelation (at longer time lags) and the integral scale are dominated by the large-scale motions which are affected by the non-physical forcing and period boundary conditions. Consequently caution is needed in relating these statistics from the simulations to those of 'natural' turbulence.

Lagrangian velocity frequency spectra, $E^{\mathrm{L}}(\omega)$, and acceleration spectra, $A^{\mathrm{L}}(\omega)$ $(\equiv \omega^2 E^{\mathrm{L}}(\omega))$, are obtained by Fourier-transforming the velocity autocorrelation. The acceleration spectra shown in figure 11 demonstrate that the noise level is well within tolerable limits: at the Kolmogorov angular frequency ω_η $(\equiv \pi/\tau_\eta)$, the spectra are typically two orders of magnitude lower than their peak values, and have a slope

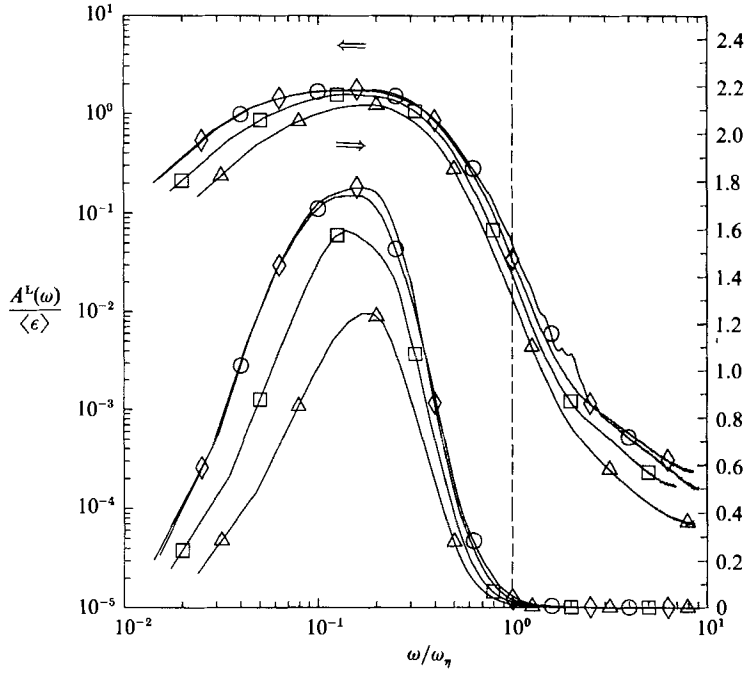

FIGURE 11. Kolmogorov-scaled acceleration frequency spectra for the 128^3 simulations, on log–log (left-side) and log–linear (right-side) scales. △, $R_\lambda = 38$; □, $R_\lambda = 63$; ○, $R_\lambda = 90$; ◇, $R_\lambda = 93$. Dashed vertical line marks the Kolmogorov frequency ω_η. The peaks give values of B_0^*.

of about -5 on log–log scales. At frequencies higher than $2\omega_\eta$, the slopes of the spectra decrease (in absolute value), indicating the presence of noise.

To highlight the separation of scales in the frequency domain, velocity and acceleration spectra, normalized by the respective variances, of the 128^3 simulations are shown together in figure 12. In each case, there is negligible energy beyond the Kolmogorov frequency, consistent with Tennekes (1975) who postulated that $E^L(\omega)$ extends only to frequencies of order ω_η. The most energetic eddies are seen to be those of characteristic time about $3T_L$ or, equivalently (see table 2), twice the eddy-turnover time T_e.

As the Reynolds number increases, the acceleration spectra are shifted towards higher frequencies (relative to π/T_L), signifying a widening timescale separation. The spectral shapes tend to be 'skewed' correspondingly. At $R_\lambda = 63$, the peak contributions to the acceleration spectra are at about $\omega_\eta/3.5$; this corresponds to a timescale of about $0.18\tau_\epsilon$, or a ratio of T_L/τ_η of 5.6. This separation is roughly of the same order as that between the scaled plots of energy and dissipation wavenumber spectra in figure 1 (§2).

It is important to confirm that the forcing scheme does not interfere with the true physical processes at the higher frequencies dominating the acceleration spectra – i.e. to show that the observed peaks in the acceleration spectra have not been contaminated by artificial forcing. In figure 12, we also show the spectrum of the forcing acceleration. This is evaluated as the frequency spectrum of a UO process of variance $4N_F\sigma^2$. (This numerical factor arises from the manner in which the forcing is implemented in the code.) Here this spectrum has been normalized by the same scaling parameters as the $R_\lambda = 38$ acceleration spectrum, and it is seen to be

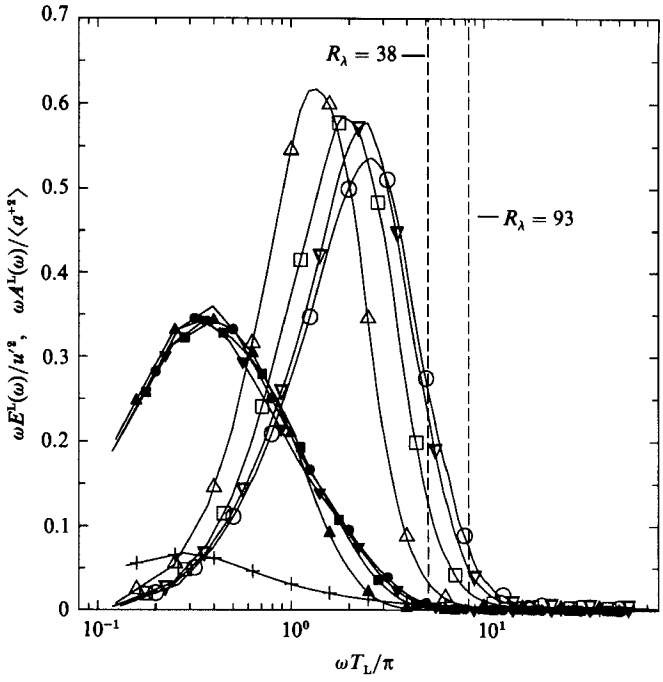

FIGURE 12. Lagrangian velocity and acceleration frequency spectra, normalized for unit area and multiplied by frequency. Plot is log–linear, with frequency scaled by integral timescale. Acceleration spectra: △, $R_\lambda = 38$; □, $R_\lambda = 63$; ○, $R_\lambda = 90$; ▽, $R_\lambda = 93$. Solid symbols for velocity spectra. Vertical dashed lines indicate the ratio T_L/τ_η for $R_\lambda = 38$ and 93 cases; +, spectrum of UO process of variance $4N_F\sigma^2$.

concentrated in the low frequencies, while much lower than the acceleration spectra in their peak frequency range. In other words, the forcing has a minimal effect on the acceleration spectra. Moreover, the case illustrated is a 'worst case' for two reasons. First, the spectrum of the IUO process used in the refined forcing scheme decays more rapidly than that of the UO process. Second, as the Reynolds number is increased, the acceleration spectra are shifted towards higher frequencies, where the effects of forcing are even less significant.

The velocity frequency spectrum $E^L(\omega)$, like the velocity autocorrelation, is determined primarily by the large-scale motions which are affected by the forcing and periodic boundary conditions. It is nevertheless interesting to observe that the spectra for different Reynolds numbers almost collapse, in marked contrast to the $E(k)$ curves in figure 1 (§2). Perhaps this indicates that the Lagrangian statistics of the large-scale motions are less contaminated by forcing than the Eulerian data.

We now examine the shape and Reynolds-number dependence of the acceleration spectra $A^L(\omega)$. The spectra shown in figure 11 are normalized by the Kolmogorov scales, so that the areas under the equivalent linear plots are proportional to a_0 (the acceleration variance $\langle a^{+2}\rangle$ normalized by v_η^2/τ_η^2). Like many other statistics, the spectra exhibit considerable statistical differences between the $R_\lambda = 90$ and $R_\lambda = 93$ cases, as a result of statistical errors (see the Appendix). Apart from this apparent anomaly, the spectra increase monotonically with Reynolds number over a wide range of frequencies: we have already seen (§4.1) that a_0 varies strongly with Reynolds number in the simulations. It is inevitable, therefore, that the spectra do

not collapse. However, it is interesting to observe that the Reynolds-number dependence extends to the highest frequencies.

According to the Kolmogorov (1941, 1962) hypotheses, at very high Reynolds number, there is an inertial range (with characteristic times, τ, $\tau_\eta \ll \tau \ll T_L$) in which the acceleration spectrum is flat:

$$A^L(\omega) = B_0\langle\epsilon\rangle, \tag{29}$$

where B_0 is a universal constant. The Reynolds numbers of the simulations are insufficient for the existence of such an inertial range: T_L/τ_η only ranges from about 5 to 8.5. Nevertheless, in figure 11, the spectra plotted on log–log scales do become flatter as the Reynolds number increases. However, the logarithmic scale is deceptive: on the log-linear scale, the same data do not display plateaus. Moreover, the maximum value of $A^L(\omega)/\langle\epsilon\rangle$ – denoted by B_0^*, and shown in figure 4 – does not appear to be approaching an asymptotic value as the Reynolds number increases.

4.3. *Velocity increments*

In this subsection we examine the statistical nature of the Lagrangian velocity increments $\Delta_\tau u^+(t) \equiv u^+(t+\tau) - u^+(t)$. One motivation is to test the basic assumptions in stochastic models for $u^+(t)$, and to guide the development of improved models. First, the statistics of $\Delta_\tau u^+(t)$ are presented: then the implications for stochastic models are discussed.

The variance of the velocity increment is, by definition, the second-order Lagrangian structure function $D_2^L(\tau)$. For any differentiable process (such as $u^+(t)$), for sufficiently small τ, $D_2^L(\tau)$ varies as τ^2. In fact, from the definition of the normalized acceleration variance a_0 (equation (24)), we have

$$\frac{D_2^L(\tau)}{v_\eta^{\,2}} = a_0(\tau/\tau_\eta)^2 \quad (\tau \ll \tau_\eta). \tag{30}$$

The structure functions are shown on figure 13. On this log–log plot a slope of 2 is observed for small τ/τ_η, in accord with (30). (This is not inevitable: this slope is extremely sensitive to numerical noise.) Since a_0 is found to vary with Reynolds number, a collapse of the curves (as predicted by Kolmogorov 1941) is not possible.

For large times ($\tau \gg T_L$), the structure function is simply twice the velocity variance. Hence, at large τ/τ_η, $D_2^L(\tau)/v_\eta^2$ equals $2u'^2/v_\eta^2$, and it is observed to increase with R_λ, as expected.

Figure 13 also shows data taken from a 64^3 calculation at $R_\lambda = 40$ previously obtained by using UO forcing and the 'TS13' interpolation scheme (Yeung & Pope 1987). The curve is close to but slightly higher than the 128^3, $R_\lambda = 38$ values. This suggests that second-order statistics in the previous study are sufficiently accurate.

According to the Kolmogorov (1941, 1962) hypotheses, at very high Reynolds numbers, for inertial subrange times ($\tau_\eta \ll \tau \ll T_L$), the structure function is

$$D_2^L(\tau) = C_0\langle\epsilon\rangle\tau, \tag{31}$$

where C_0 is a universal constant. Figure 14 shows $D_2^L(\tau)/(\langle\epsilon\rangle\tau)$ plotted against τ/τ_η. If (31) held, then the curves in figure 14 would show plateaus of height C_0. Not surprisingly, at the moderate Reynolds numbers simulated, such plateaus are not observed. Furthermore, the maximum value of $D_2^L(\tau)/(\langle\epsilon\rangle\tau)$ – denoted by C_0^* and plotted against R_λ in figure 4 – does not appear to be approaching an asymptotic value.

In incompressible homogeneous turbulence, the one-point, one-time joint p.d.f. of

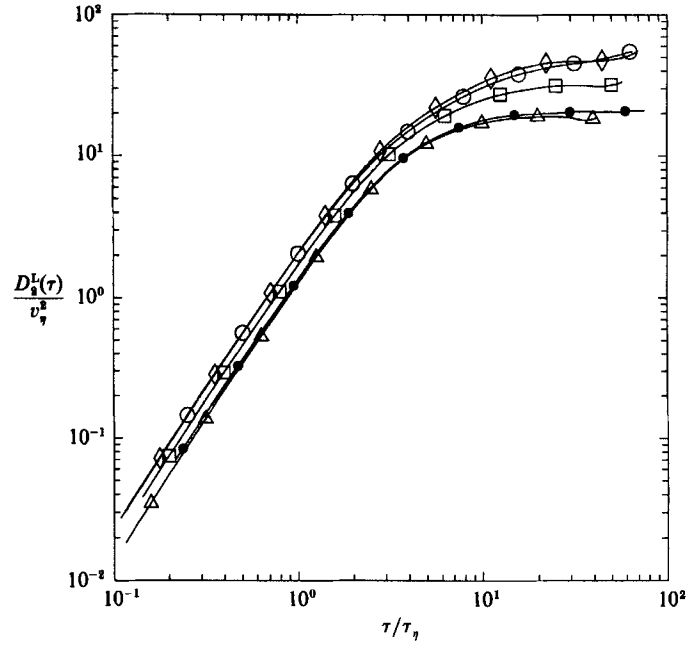

FIGURE 13. Second-order Lagrangian velocity structure functions $D_2^L(\tau)$ under Kolmogorov scaling. Open symbols for the 128^3 simulations: △, $R_\lambda = 38$; □, $R_\lambda = 63$; ○, $R_\lambda = 90$; ◇, $R_\lambda = 93$; ●, $R_\lambda = 40$ on 64^3 grid, from previous data of Yeung & Pope (1987).

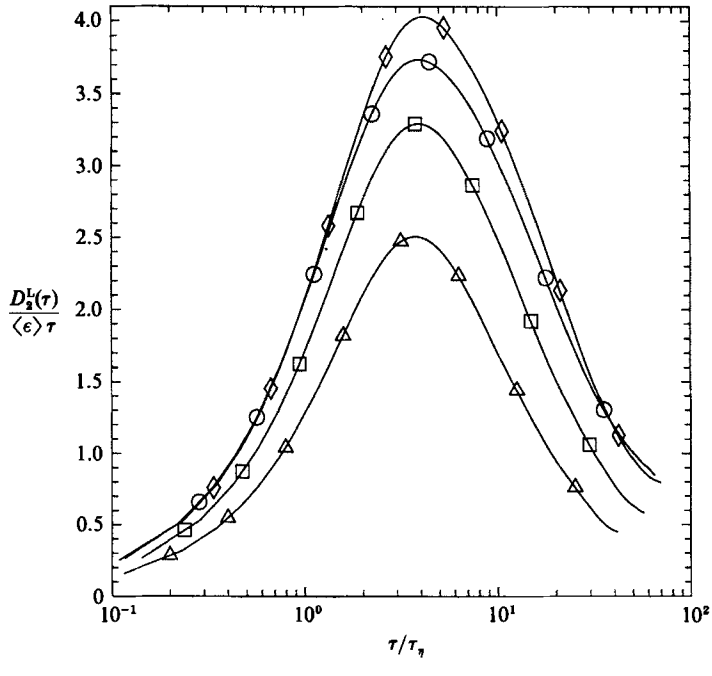

FIGURE 14. Second-order structure functions $D_2^L(\tau)$ normalized by $\langle\epsilon\rangle\tau$, against Kolmogorov-scaled time lag, for the 128^3 simulations. △, $R_\lambda = 38$; □, $R_\lambda = 63$; ○, $R_\lambda = 90$; ◇, $R_\lambda = 93$. The peaks of the curves give C_0^* for each simulation.

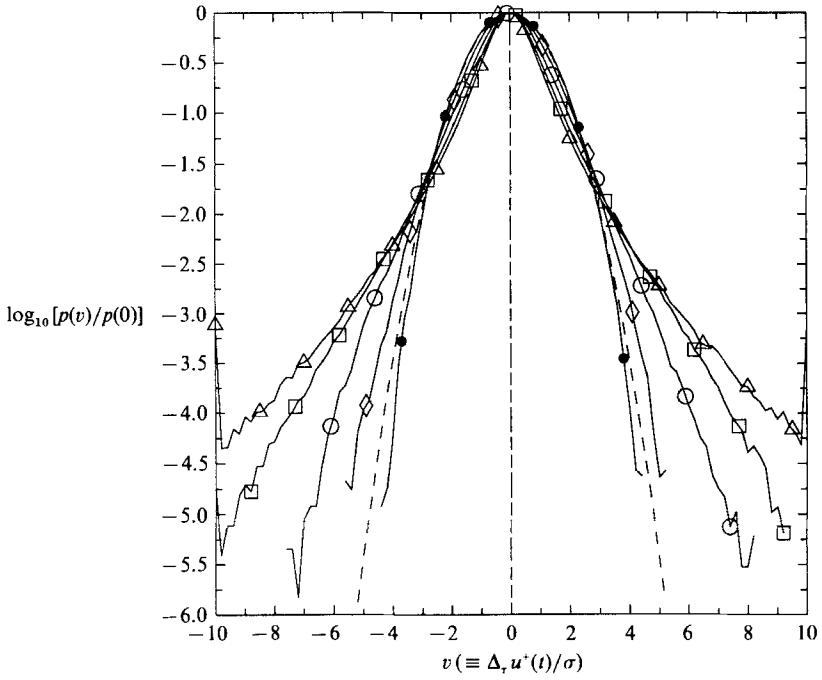

FIGURE 15. Base-10 logarithms of standardized p.d.f.'s of velocity increments at several time lags for the 128^3, $R_\lambda = 93$ simulation. τ/τ_η ($\approx \tau/8h$): △, $\frac{1}{2}$; □, 2; ○, 4; ◇, 8; ●, 32. Dashed curve (parabolic) denotes the standard Gaussian density.

the Eulerian (and Lagrangian) velocity is Gaussian (see e.g. Tavoularis & Corrsin 1981*a*): but the fine-scale structure is known to be non-Gaussian. Despite ample experimental evidence (e.g. Tavoularis & Corrsin 1981*b*; Anselmet *et al.* 1984) for the intermittent and non-Gaussian character of Eulerian velocity gradients, little is known of the intermittency of Lagrangian small-scale turbulence components, such as the velocity increments over short time intervals. The simulation results confirm the expectation that such Lagrangian statistics are also highly intermittent and non-Gaussian.

Figure 15 shows the logarithms of the standardized p.d.f.'s $p(v)$ of the velocity increments $\Delta_\tau u^+(t)$, at different time lags τ, obtained from the $R_\lambda = 93$ simulation. These p.d.f.'s are roughly symmetric. At the longest time lag shown ($\tau \approx 32\tau_\eta$) the p.d.f. appears to be Gaussian (i.e. $\ln[p(v)] \propto -v^2$), consistent with the Gaussianity of the one-point, one-time p.d.f. of velocity. At the intermediate time lags ($\tau \approx 2\tau_\eta$ and $\tau \approx 4\tau_\eta$) non-Gaussian behaviour is evident: $\ln[p(v)]$ appears to decay as $-|v|$. For small time lags ($\tau \approx \frac{1}{2}\tau_\eta$ and $\tau \approx \frac{1}{8}\tau_\eta$ (not shown)), the decay rates are possibly even slower than $\ln[p(v)] \propto -|v|$. Wide tails indicating intermittency are seen to extend up to 10 standard deviations and beyond. In all respects these observations are similar to those made by Anselmet *et al.* (1984), who measured the p.d.f. of the spatial velocity increment $[\boldsymbol{u}(\boldsymbol{x}+\Delta\boldsymbol{x}, t)-\boldsymbol{u}(\boldsymbol{x}, t)]$ in an asymmetric jet with $R_\lambda = 536$.

The flatness factor provides a quantitative measure of departure from Gaussianity. For very small time lags, the flatness factor of the velocity increment approaches that of the acceleration components, requiring an accurate calculation of the acceleration fourth moment. Well-defined values can be obtained from the simulations only if numerical noise in the time series is at an insignificant level. This thus provides a rigorous test of numerical accuracy.

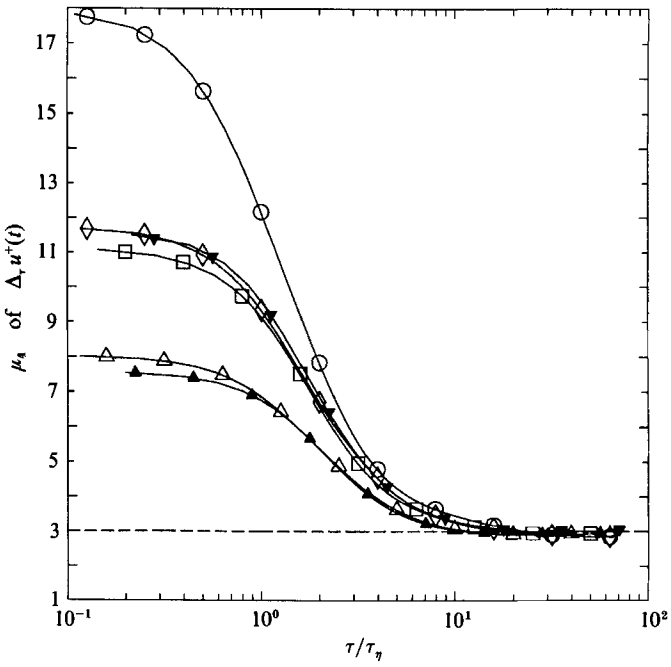

FIGURE 16. Flatness factors of velocity increments, against Kolmogorov-scaled time lag. Open symbols for 128^3 simulations: △, $R_\lambda = 38$; □, $R_\lambda = 63$; ○, $R_\lambda = 90$; ◇, $R_\lambda = 93$. 64^3 cases (see §4.3): ▲, '64A'; ▼, '64B'. Dashed line denotes Gaussian values.

Figure 16 shows the velocity-increment flatness factors, as functions of the Kolmogorov-scaled time lag. First we use these data to address the question of numerical accuracy. Two sets of 64^3 data are compared with the 128^3 $R_\lambda = 38$ data, and, for convenience, are referred to as cases '64A' and '64B' here. Apart from grid size (hence spatial resolution), the conditions of case 64A differ from the 128^3 simulation only in the use of a slower sampling rate ($h \approx \frac{1}{4}\tau_\eta$) and fewer particles (1600). For case '64B' (taken from Yeung & Pope 1987), the differences include, in addition, (*a*) the use of UO process for forcing, and (*b*) a Taylor-series interpolation scheme which, although sufficiently adequate, does not guarantee continuous approximations to the fluid particle velocity (see Yeung & Pope 1988).

Although only at slightly higher Reynolds number ($R_\lambda = 40$), case 64B gives flatness factors much higher than those of the 128^3, $R_\lambda = 38$ simulation (and case 64A). This over-estimation can only be attributed to the numerics. Sampling rate and number of particles (i.e. statistical error) are ruled out as possible factors since they are the same for 64A and 64B. The explanation lies in the use of UO forcing and the Taylor-series interpolation scheme for 64B, resulting in non-differentiability of the acceleration and higher levels of numerical noise. This also explains the anomaly in Reynolds-number trend in the previous calculations (Yeung & Pope 1987).

It is reassuring to observe that the 64A data, at $k_{\max}\eta = 1.5$, differ only slightly from the 128^3 simulation at $k_{\max}\eta = 3.0$ of the same Reynolds number. This means that with $k_{\max}\eta = 1.5$, the spatial resolution is adequate for fourth-order statistics: hence the $R_\lambda = 63$ data can be trusted.

Since the $R_\lambda = 90$ and 93 cases are statistically identical, the observed differences in the flatness factors at small time lags (approximately 12 and 18) indicate significant statistical errors. These are the largest statistical errors in the results

reported, and are analysed and discussed further in the Appendix. (It should be noted that statistical errors in second-order quantities are much smaller: in a_0 it is most likely less than 2% – see table 2.)

We now return to the physical significance of the results shown in figure 16. As expected, the flatness factors take values far higher than the Gaussian value (3) for short times lags, with a considerable increase with Reynolds number indicated by the 128^3 simulations. Since the one-time p.d.f. of velocity is Gaussian, it is inevitable that, as observed, the flatness factor of $\Delta_\tau u^+(t)$ tends to 3 for sufficient large τ. The Gaussian value is reached at a time lag of roughly 10–20 Kolmogorov scales, which is also about 2 Lagrangian integral timescales.

We next discuss the significance of the velocity increment statistics for stochastic models. As mentioned in the Introduction, stochastic models for the velocity of a fluid particle have been used in studies of dispersion (e.g. Reid 1979), and also as the basis for the calculation of inhomogeneous turbulent flow fields (e.g. Haworth & Pope 1987).

The simplest and most widely used of these stochastic models is the Langevin equation. When applied to the case of statistically stationary isotropic turbulence, it models the velocity increment $\Delta_\tau u^+(t)$ as a Gaussian random variable with zero mean and variance

$$D_2^{\mathrm{L}}(\tau) = C_0 \langle \epsilon \rangle \tau_0(\tau), \tag{32}$$

where the function τ_0 is defined by

$$\begin{aligned} \tau_0(\tau) &\equiv \tfrac{1}{2} T_{\mathrm{L}} [1 - \exp(-2\tau/T_{\mathrm{L}})] \\ &= \tau(1 + O(\tau/T_{\mathrm{L}})). \end{aligned} \tag{33}$$

The autocorrelation function is

$$\rho_{\mathrm{L}}(\tau) = \exp(-|\tau|/T_{\mathrm{L}}), \tag{34}$$

and the integral timescale is given by

$$T_{\mathrm{L}} = \tau_\epsilon / (\tfrac{3}{4} C_0) \tag{35}$$

(where $\tau_\epsilon \equiv \frac{1}{2} q^2 / \langle \epsilon \rangle$).

The utility of this model is that $\boldsymbol{u}^+(t)$ is modelled as a simple (vector) Markov process. Because of this, however, it is physically unrealistic at high frequencies. Four equivalent manifestations of the qualitatively incorrect behaviour are: the modelled process $u^+(t)$ is not differentiable; for small τ, the structure function varies as τ rather than as τ^2; the autocorrelation has discontinuous slope at the origin; and, the acceleration spectrum tends to a non-zero constant as the frequency tends to infinity.

Despite these limitations, a Markov process such as that generated by the Langevin equation might provide a realistic model of $\boldsymbol{u}^+(t)$ (in high-Reynolds-number turbulence) when viewed on timescales greater than τ_η (or frequencies lower than ω_η). However, the data from the simulations do not support the Langevin equation in two respects. First, although the predicted structure function (equation (32)) is in accord with the Kolmogorov hypotheses (in the inertial range), it is qualitatively different from those observed in figure 14. This difference, however, may be attributed to the moderate Reynolds numbers of the simulations. Second, contrary to the assumption of the Langevin model, the increments of $\Delta_\tau u^+(t)$ are observed to be non-Gaussian.

The Langevin equation can be modified to account for internal intermittency. In the spirit of Kolmogorov's (1962) refined hypotheses, the infinitesimal increment $\mathrm{d}u^+(t)$ can be made to depend on the local value of dissipation. Specifically, $\mathrm{d}u^+(t)$

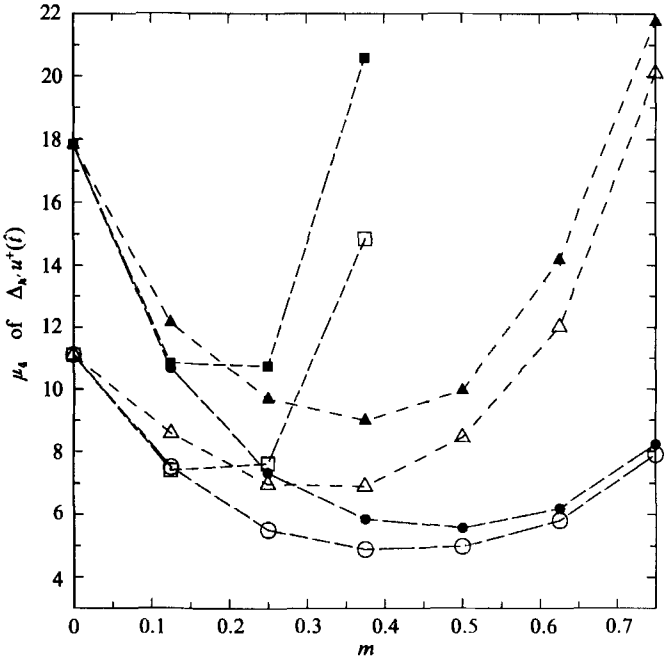

FIGURE 17. Flatness factors of velocity increments at smallest time lag (h') in stretched time $\hat{t}$, against the time-stretching exponent (m), for the 128^3, $R_\lambda = 63$ (open symbols) and $R_\lambda = 90$ (solid symbols) simulations. Stretching variable: △, ϵ^+; □, ζ^+; ○, φ^+.

(given $\epsilon^+(t)$) can be hypothesized to be a Gaussian random variable with conditional variance $C_0\epsilon^+(t)\,\mathrm{d}t$. This hypothesis implies that the DNS time series $u^+(\hat{t})$ is Gaussian in stretched time $\hat{t}$, where $\hat{t} = (\epsilon^+/\langle\epsilon\rangle)^{\frac{1}{2}}\,\mathrm{d}t$.

To test a generalization of the above hypotheses, the time series $u^+(t)$ are transformed into stretched time (equation (27)) based on the invariants ϵ^+, ζ^+ or φ^+, with a general exponent m. (The above hypothesis corresponds to the choice of ϵ^+ and $m = \frac{1}{2}$.) Figure 17 shows the resulting flatness factors of $\Delta_{h'}u^+(\hat{t})$ (where h' is the smallest increment in $\hat{t}$) – essentially the same as the flatness factors of $\mathrm{d}u^+(\hat{t})/\mathrm{d}\hat{t}$ – for the $R_\lambda = 63$ and 90 simulations. It may be seen that the pseudo-dissipation φ^+ (rather than ϵ^+) is most successful in reducing the flatness factor, and with the choice $m = \frac{1}{2}$ a minimum value of approximately 5.5 is obtained. Moreover, besides yielding flatness factors not too far from the Gaussian value of 3, this scaling (based on φ^+ and $m = \frac{1}{2}$) is effective in greatly reducing the dependence on R_λ (see *Note added in proof* on p. 584). A stochastic model for $\boldsymbol{u}^+(t)$ based on this scaling is described by Pope (1988*b*).

Even though the scaling is successful in reducing the flatness factor and its Reynolds-number dependence, large velocity increments (in stretched time) are still found to be significantly more probable than if they were Gaussian. This may be observed directly in figure 18 which shows the logarithm of the standardized p.d.f. of velocity increments in stretched time. As with the velocity increments in regular time (figure 15), for time intervals less than $5\tau_\eta$, the p.d.f. appears to decay as $\ln p(v) \propto -|v|$.

Finally a comment is called for on the value of C_0 used in the Langevin model. Recall that at high Reynolds number and for inertial subrange times τ ($\tau_\eta \ll \tau \ll T_\mathrm{L}$), according to both the Kolmogorov hypotheses (1941, 1962) and the Langevin

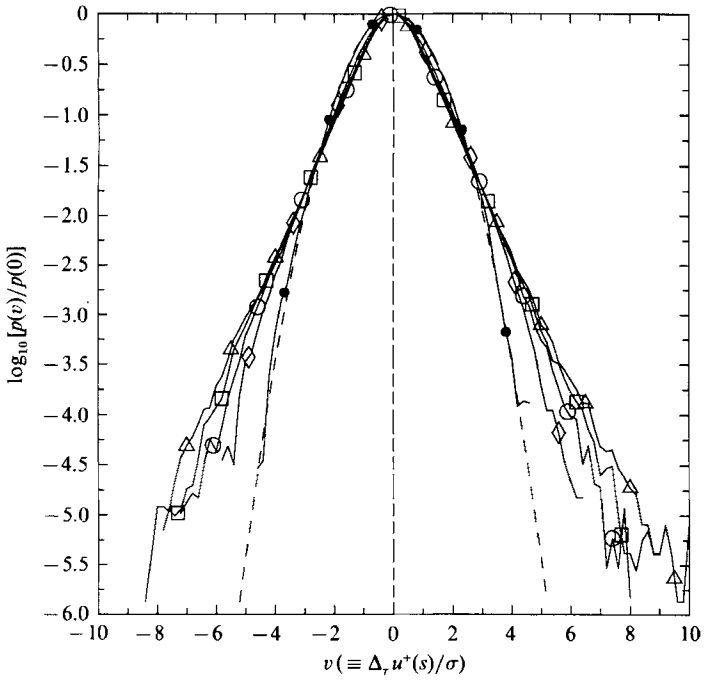

FIGURE 18. Same as figure 15, but for velocity increments in stretched time, based on φ^+ and $m = \frac{1}{2}$.

equation, the quantity $D_2^{\mathrm{L}}(\tau)/(\langle\epsilon\rangle\tau)$ adopts a constant value, C_0. As already mentioned, such a constant value is not observed in our simulations (figure 14) – quite possibly because of moderate Reynolds number – but the peak value of $D_2^{\mathrm{L}}(\tau)/(\langle\epsilon\rangle\tau)$, denoted by C_0^*, increases as $R_\lambda^{\frac{1}{2}}$, to a value of about 4 at $R_\lambda \approx 90$. It is reasonable to suppose, therefore, that if $D_2^{\mathrm{L}}(\tau)/(\langle\epsilon\rangle\tau)$ does adopt a constant value at high Reynolds number, then this value is greater than 4.

On the other hand, Anand & Pope (1985) deduced the value $C_0 = 2.1$ by comparing dispersion calculations using the Langevin equation with Warhaft's (1984) experimental data, for which $R_\lambda \approx 45$. Clearly, 2.1 is not the high-Reynolds-number asymptotic value.

4.4. *Acceleration, dissipation, enstrophy and pseudo-dissipation*

This subsection is devoted to a discussion of the statistical properties of the acceleration magnitude $|\boldsymbol{a}^+|(t)$, the mechanical dissipation $\epsilon^+(t)$, enstrophy $\zeta^+(t)$ and pseudo-dissipation $\varphi^+(t)$, based on 128^3 simulation data. All of these quantities pertain to the small-scale turbulence structure, and thus contain physical information on intermittency. Summaries of numerical data are given in tables 3–5.

Since φ^+ is the arithmetic mean of ϵ^+ and ζ^+ (equation (20)), the mean values shown in table 3 are not independent. The small observed differences between $\langle\epsilon^+\rangle$ and $\langle\varphi^+\rangle$ indicate a small statistical error (equation (21)). All the quantities exhibit large fluctuations. For ϵ^+ and φ^+ the standard deviation is approximately equal to the mean, while for ζ^+ it is typically 50% greater. That is, vorticity (or enstrophy) is more intermittent than strain rate (or dissipation).

Oboukhov (1962) proposed a model of log-normal distribution for dissipation fluctuations: a detailed account can be found in Monin & Yaglom (1975). It has been

	$\|a^+\|(t)$	$\epsilon^+(t)$	$\zeta^+(t)$	$\varphi^+(t)$
$\bar{x}$†	§	2.654	2.654	2.654
		0.766	0.756	0.761
		0.772	0.771	0.771
		2.644	2.657	2.650
		0.781	0.795	0.788
		0.885	0.892	0.888
$\sigma/\bar{x}$†	0.683	0.997	1.369	0.998
	0.722	1.070	1.466	1.086
	0.689	1.007	1.447	1.041
	0.769	1.091	1.537	1.131
	0.856	1.211	1.924	1.360
	0.774	1.109	1.655	1.197
T_i/T_L‡	0.62	0.55	1.00	0.88
	0.64	0.49	0.94	0.80
	0.56	0.45	0.95	0.82
	0.61	0.48	0.87	0.79
	0.59	0.48	0.77	0.75
	0.58	0.46	0.80	0.74

† $\bar{x}$ and σ denote sample mean and standard deviation.

‡ T_i is the integral timescale of the representative variable. Preprocessed data (see Appendix) are used in the $R_\lambda = 54$, 59 and 90 cases.

§ The mean value of $|a^+|$ is omitted.

TABLE 3. Acceleration, dissipation, enstrophy and pseudo-dissipation. (Each entry is of six parts, for $R_\lambda = 38$, 54, 59, 63, 90 and 93 successively.)

further postulated (Monin & Yaglom 1975, p. 615) that the model can also be applied to other positive scalar quantities characterizing the small scales. The acceleration magnitude, enstrophy and pseudo-dissipation all fall in this category. A number of experimental (e.g. Antonia, Satyaprakash & Hussain 1982) and numerical (e.g. Kerr 1985) studies have addressed the accuracy of the log-normal model. However, most studies focus on the model's predictions for single components of the velocity gradient tensor. Published data which examine directly the p.d.f. of dissipation or its logarithm (let alone $|a^+|(t)$, $\zeta^+(t)$ or $\varphi^+(t)$) still appear to be lacking.

It is straightforward to use the Lagrangian time series to obtain accurate estimates of the p.d.f.'s of the logarithms of $|a^+|(t)$, $\epsilon^+(t)$, $\zeta^+(t)$ and $\varphi^+(t)$, and their moments. High sampling accuracy can be expected since, in view of stationarity and homogeneity, the number of samples (number of sampled time levels times number of particles) is in the range of 2×10^6. Figure 19 shows on a logarithmic scale, for the $R_\lambda = 90$ simulation, the standardized p.d.f.'s of the logarithms of $|a^+|$, ϵ^+, ζ^+ and φ^+. Each p.d.f. is normalized by its value at the mean, and – to bring out the differences – multiplied by the respective variance. Gaussian distributions with the same variances are indicated by the dashed lines (which are parabolas). Thus, if the quantities under consideration were log-normally distributed, on figure 19, the p.d.f.'s would coincide with the dashed lines.

It is evident from figure 19 that while the p.d.f. of $\ln\varphi^+$ appears symmetric, the others are negatively skewed (see skewness coefficients μ_3 in table 4), indicating a relatively high probability of low values. Turn-ups at the lefts ends of the p.d.f.'s represent very small values falling outside the sampling range. The absence of such turn-ups at the right ends shows that very large values are less probable.

The first four, and the sixth, central moments of the logarithms are listed in table

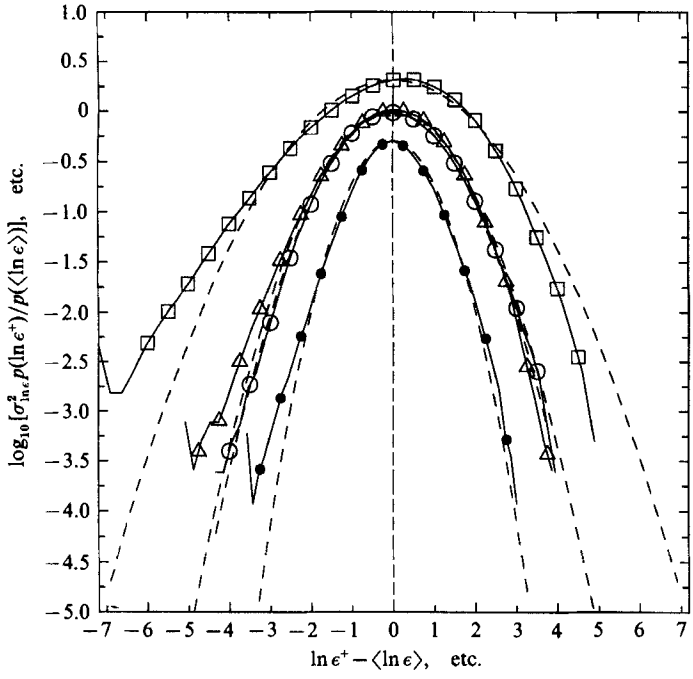

FIGURE 19. Standardized p.d.f.'s of $\ln\epsilon^+$, $\ln\zeta^+$, $\ln\varphi^+$ and $\ln|\boldsymbol{a}^+|$, for the 128^3, $R_\lambda = 90$ simulation. Base-10 logarithm of the p.d.f. normalized by the value at the mean and multiplied by the variance, is shown against departure from mean value. △, $\ln\epsilon^+$; □, $\ln\zeta^+$; ○, $\ln\varphi^+$; ●, $\ln|\boldsymbol{a}^+|$. The p.d.f.'s extend to ± 5 standard deviations for each variable. Dashed curves (parabolic) denote standard Gaussian densities.

4. If a random variable ϕ is log-normally distributed, then $\ln\phi$ has normalized central moments μ_3, μ_4 and μ_6 equal to 0, 3 and 15 respectively. The tabulated moments show that the pseudo-dissipation φ^+ is almost perfectly log-normal, even at our modest Reynolds numbers, but that $|\boldsymbol{a}^+|$, ϵ^+ and ζ^+ show varying degrees of departure from log-normality. The departure is slight for dissipation, but more marked for acceleration and enstrophy, as inferred from the p.d.f. plots.

The argument for the log-normal model depends on the scale separation between large and small scales, which widens with increasing Reynolds numbers. In table 4, moments of $\ln\epsilon^+$ and $\ln\zeta^+$ become closer to the Gaussian values as R_λ increases from 38 to 93. It is possible, therefore, that the distribution becomes log-normal in the high-Reynolds-number limit for all four variables.

Kolmogorov (1962) also assumed that $\sigma^2_{\ln\epsilon}$ varies linearly with the logarithm of the ratio L/η, where L is a lengthscale of the large eddies. Noting that L/η is a power of R_λ (irrespective of the specific choice of L, say L_1 or L_ϵ), by stationarity and homogeneity we may expect a relationship of the form

$$\sigma^2_{\ln\epsilon} = a + b\ln R_\lambda \tag{36}$$

(where a and b are constants for the flows simulated). Figure 20 shows that, within the limits of statistical scatter, this appears to hold for the all the three invariants, as well as acceleration magnitude. Approximate values of the coefficients a and b for each variable are given under this figure. It may be noted that the value of b is 80% higher for enstrophy than for dissipation.

The approximate log-normality found for the three invariants leads to the

	$\ln\|\boldsymbol{a}^+\|(t)$	$\ln\epsilon^+(t)$	$\ln\zeta^+(t)$	$\ln\varphi^+(t)$
$\bar{x}$†	1.973	0.588	0.286	0.623
	1.241	−0.690	−1.023	−0.669
	1.281	−0.670	−1.019	−0.651
	2.283	0.541	0.192	0.558
	1.508	−0.740	−1.124	−0.733
	1.664	−0.576	−0.972	−0.572
σ^2	0.427	0.828	1.656	0.714
	0.432	0.898	1.783	0.797
	0.412	0.888	1.835	0.799
	0.467	0.910	1.860	0.831
	0.510	1.031	2.066	0.970
	0.472	0.966	2.036	0.910
μ_3	−0.25	−0.24	−0.52	−0.04
	−0.18	−0.22	−0.50	−0.03
	−0.22	−0.26	−0.50	−0.05
	−0.16	−0.19	−0.47	0.01
	−0.02	−0.06	−0.39	0.06
	−0.12	−0.21	−0.44	−0.00
μ_4	3.55	3.22	3.60	3.04
	3.58	3.23	3.56	3.08
	3.54	3.17	3.51	2.94
	3.45	3.15	3.53	3.00
	3.47	3.12	3.41	3.02
	3.47	3.14	3.44	3.00
μ_6	26.5	20.0	28.8	15.9
	26.2	19.8	27.9	16.2
	25.8	19.4	27.0	14.3
	23.5	18.5	27.1	15.1
	23.1	17.6	23.7	15.5
	23.9	18.1	24.8	15.5
T_i/T_L‡	0.62	0.60	0.97	0.96
	0.57	0.56	0.97	0.93
	0.51	0.52	0.91	0.89
	0.64	0.57	0.90	0.92
	0.59	0.58	0.84	0.90
	0.57	0.58	0.86	0.91

TABLE 4. Acceleration, dissipation, enstrophy and pseudo-dissipation (logarithms). (For notation, see table 3.)

question of whether their logarithms are also approximately joint-normal. Bivariate, standardized, joint p.d.f's between the logarithms obtained from the simulations show that they are not. Figures 21–23 show the contour plots of the joint p.d.f's, at $R_\lambda = 90$. The contours clearly differ from the ellipses of joint-normal random variables, markedly so for the pairs $(\ln\epsilon^+, \ln\varphi^+)$ and $(\ln\zeta^+, \ln\varphi^+)$. Especially for these two pairs, all contours are concentrated in the first and third quadrants, indicating that the three invariants are (on the average) likely to take high or low values simultaneously.

The $\ln\epsilon^+$–$\ln\zeta^+$ isoprobability contours (figure 21) appear to be roughly symmetric about the 45° line crossing the first and third quadrants at the origin. This means that local strain and vorticity are about equally likely to exceed each other in magnitude. Looking along this line, the contours become gradually narrower. This

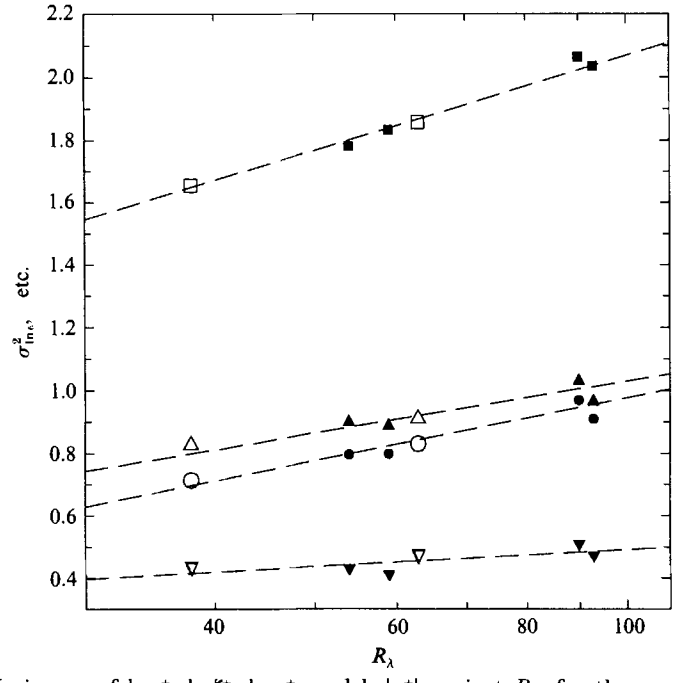

FIGURE 20. Variances of $\ln\epsilon^+$, $\ln\zeta^+$, $\ln\varphi^+$, and $\ln|a^+|$ against R_λ, for the same simulations as in figure 4. Open symbols for $K_F/k_0 = 2\sqrt{2}$, solid symbols for $K_F/k_0 = \sqrt{2}$. Dashed lines of the form $\sigma^2 = a + b\ln R_\lambda$ indicate approximate Reynolds-number dependence. △, $\ln\epsilon^+$, $a = -0.066$, $b = 0.238$; □, $\ln\zeta^+$, $a = 0.071$, $b = 0.434$; ○, $\ln\varphi^+$, $a = -0.354$, $b = 0.289$; ▽, $\ln|a^+|$, $a = 0.128$, $b = 0.079$.

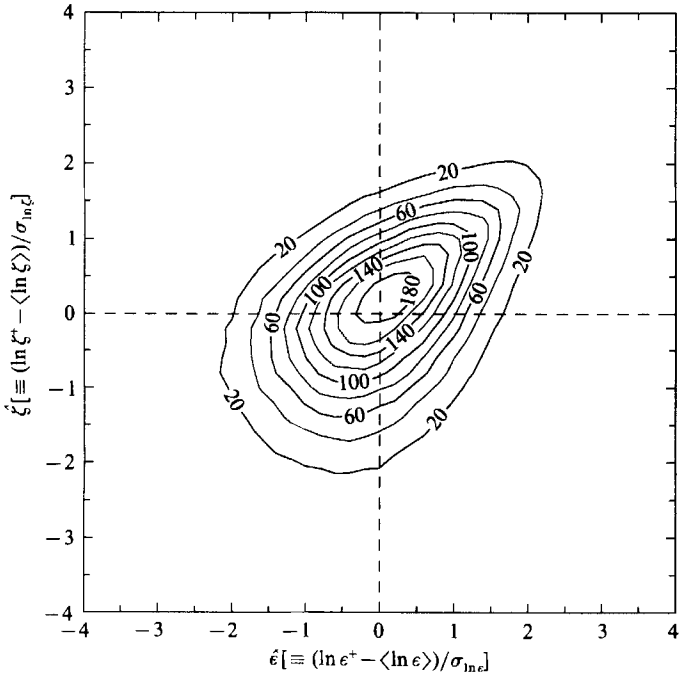

FIGURE 21. Isoprobability contours of the standardized joint p.d.f. of $\ln\epsilon^+$ and $\ln\zeta^+$, for the 128^3, $R_\lambda = 90$ simulation. Each variable ranges between ± 4 standard deviations. Contour levels start from 0.02, in intervals of 0.02 (but shown magnified by 1000).

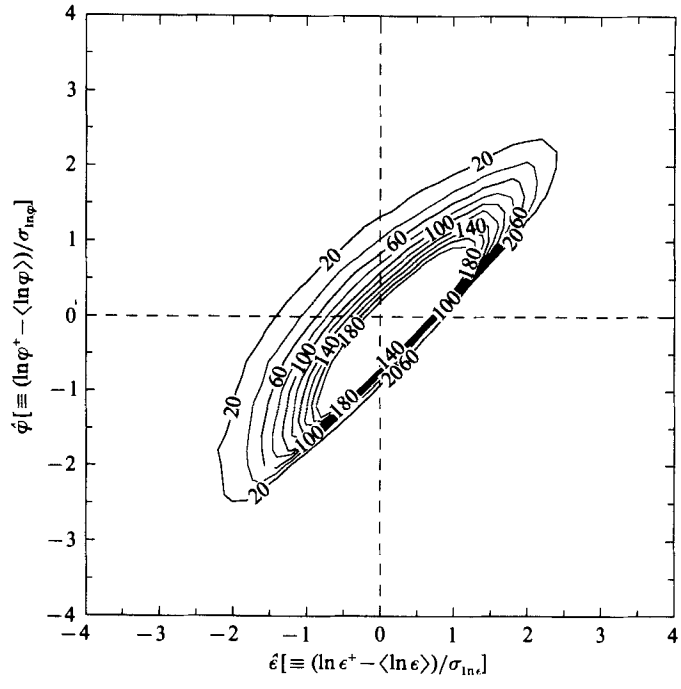

FIGURE 22. Same as figure 21, but for the joint p.d.f. of $\ln\epsilon^+$ and $\ln\varphi^+$.

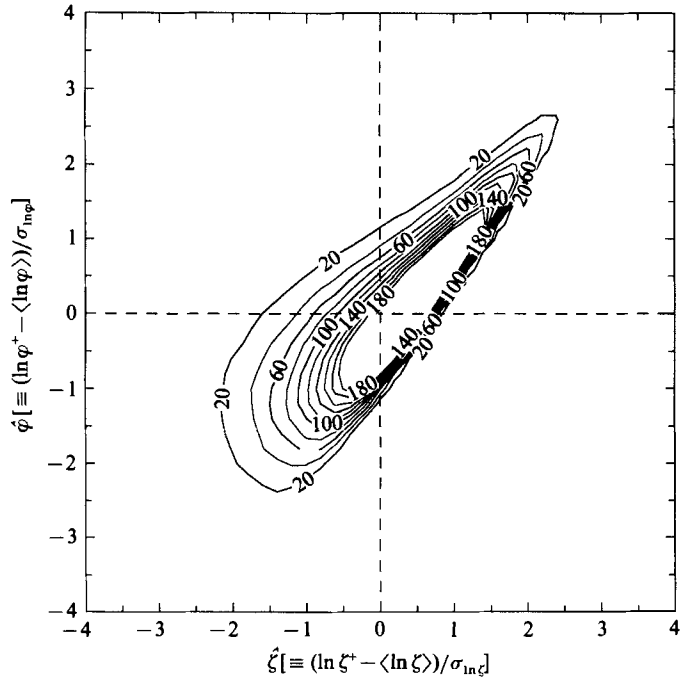

FIGURE 23. Same as figure 21, but for the joint p.d.f. of $\ln\zeta^+$ and $\ln\varphi^+$.

	$R_\lambda = 38$	$R_\lambda = 63$	$R_\lambda = 90$†	$R_\lambda = 93$
$\rho(\epsilon^+, \zeta^+)$	0.410	0.462	0.469	0.475
$\rho(\epsilon^+, \varphi^+)$	0.779	0.794	0.775	0.790
$\rho(\zeta^+, \varphi^+)$	0.890	0.902	0.921	0.913
$\rho(\ln\epsilon^+, \ln\zeta^+)$	0.322	0.386	0.438	0.412
$\rho(\ln\epsilon^+, \ln\varphi^+)$	0.784	0.810	0.835	0.822
$\rho(\ln\zeta^+, \ln\varphi^+)$	0.777	0.794	0.806	0.800
$\rho(\lvert\boldsymbol{a}^+\rvert, \epsilon^+)$	0.324	0.368	0.402	0.382
$\rho(\lvert\boldsymbol{a}^+\rvert, \zeta^+)$	0.414	0.430	0.446	0.432
$\rho(\lvert\boldsymbol{a}^+\rvert, \varphi^+)$	0.446	0.470	0.496	0.476
$\rho(\ln\lvert\boldsymbol{a}^+\rvert, \ln\epsilon^+)$	0.323	0.365	0.388	0.385
$\rho(\ln\lvert\boldsymbol{a}^+\rvert, \ln\zeta^+)$	0.296	0.321	0.335	0.328
$\rho(\ln\lvert\boldsymbol{a}^+\rvert, \ln\varphi^+)$	0.423	0.454	0.467	0.465

† Preprocessed data (see Appendix) are used for the $R_\lambda = 90$ case.

TABLE 5. Cross-correlation coefficients (128^3 simulations)

indicates that the correlation between strain and vorticity is strong when both are large, but weak when both are small. In fact, in the third quadrant, where both variables are less than their mean values, the contours resemble those of the joint p.d.f. of two independent Gaussian random variables (i.e. concentric circles).

The other two sets of p.d.f. contours (figures 22 and 23) exhibit steep contour gradients near a line of positive slope, and appear bounded by it on the right. This is because of the impossibility of either $\ln\epsilon^+$ or $\ln\zeta^+$ exceeding $\ln\varphi^+$. The similarity between the first and third quadrant segments of the $\ln\epsilon^+$–$\ln\varphi^+$ contours indicates that simultaneously high and simultaneously low values of $\ln\epsilon^+$ and $\ln\varphi^+$ are about equally probable. In contrast, the 'pointedness' of the $\ln\zeta^+$–$\ln\varphi^+$ contours show that high pseudo-dissipation is more likely to be a result of high enstrophy than dissipation.

Correlation coefficients between any two of the three invariants, and between their logarithms, are given in table 5. For the invariants, using (2), these coefficients may be readily linked to the individual variances. Thus, owing to the considerable temporal variations of volume-averaged quantities in simulations using only 18 forced modes, the $R_\lambda = 90$ values may be inaccurate for the invariants (while the logarithms are much less affected). Excepting this statistical uncertainty, the coefficients appear to increase with R_λ. (Of course, being bounded by unit, the correlation coefficients cannot increase indefinitely.)

We now consider the two-time correlation behaviour of acceleration magnitude and the three invariants (ϵ^+, ζ^+ and φ^+), by studying correlation functions and integral timescales (see tables 3 and 4). In figure 24, we show the autocorrelations for the $R_\lambda = 90$ case. The velocity autocorrelation, $\rho_L(\tau)$, is included for comparison. All are essentially non-negative at all time lags, and have shapes similar to that of $\rho_L(\tau)$. The dissipation autocorrelation function decreases with time lag most rapidly, followed by the acceleration magnitude. Dissipation and acceleration magnitude are characterized by shorter timescales: their integral scales are about 0.5 and 0.6 of the Lagrangian integral timescale T_L respectively, with no strong Reynolds-number dependence in our simulations.

The autocorrelations of acceleration components a^+ (figure 7) and acceleration magnitude $|\boldsymbol{a}^+|$ are obviously very different in character. Each component $a^+(t)$ is the

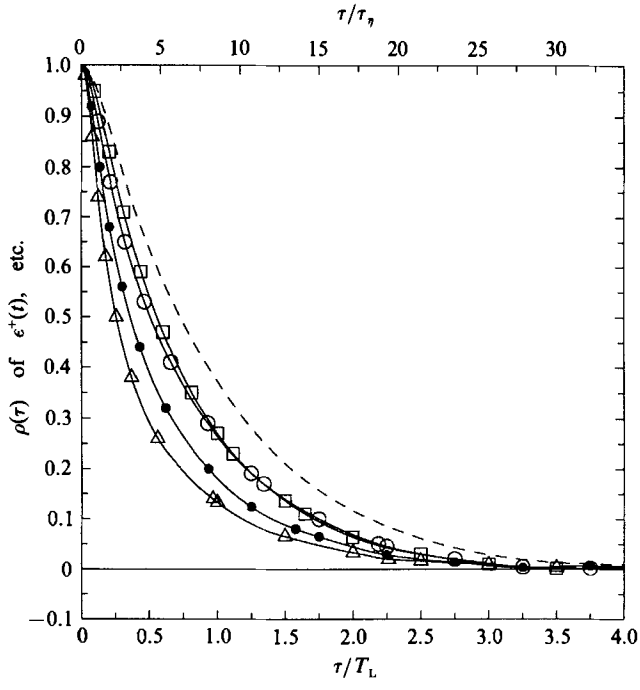

FIGURE 24. Autocorrelation functions of $\epsilon^+(t)$, $\zeta^+(t)$, $\varphi^+(t)$ and $|\boldsymbol{a}^+|(t)$, for the 128^3, $R_\lambda = 90$ simulation. Dashed line represents the Lagrangian velocity autocorrelation function $\rho_L(\tau)$. Time lag is normalized by both T_L and τ_η. △, $\epsilon^+(t)$; □, $\zeta^+(t)$; ○, $\varphi^+(t)$; ●, $|\boldsymbol{a}^+|(t)$.

derivative of a stationary process, thus its autocorrelation must be negative over a range of time lags, in order to attain a zero integral scale. As stated before (§4.1), a characteristic timescale of a^+ is the zero-crossing time τ_a, which is found to scale with τ_η ($\tau \approx 2.2\tau_\eta$). In contrast, $|\boldsymbol{a}^+|(t)$ is not the derivative of a stationary process, and its integral timescale $T_{|\boldsymbol{a}^+|}$ is positive. Its autocorrelation remains significantly positive up to about $2T_L$ and its integral timescale is about $0.6T_L$.

The difference between these acceleration timescales is reconciled as follows. The acceleration vector $\boldsymbol{a}^+(t)$ can be written as $|\boldsymbol{a}^+|(t)\,\boldsymbol{e}^+(t)$, where $\boldsymbol{e}^+(t)$ is a time-dependent unit vector in the direction of $\boldsymbol{a}^+(t)$. For $|\boldsymbol{a}^+|$ to have a timescale significantly greater than that of a^+ (about $2\tau_\eta$) implies that the timescale of the components of $\boldsymbol{e}$ must also be of order $2\tau_\eta$. This has been confirmed directly. Thus the magnitude of acceleration changes slowly (on a timescale of approximately $0.6T_L$), while its orientation changes more rapidly (on a timescale of order $2\tau_\eta$). (At the highest Reynolds number simulated the ratio $(0.6T_L)/(2\tau_\eta)$ is only 2.4. But it is significant that $T_{|\boldsymbol{a}^+|}$ scales with T_L, while τ_a scales with τ_η.)

Although they are small-scale quantities, like $|\boldsymbol{a}^+|(t)$, the invariants $\ln\epsilon^+(t)$, $\ln\zeta^+(t)$ and $\ln\varphi^+(t)$ have substantial integral timescales that scale with T_L instead of τ_η. This may be understood by recognizing that the autocorrelations are dominated by the intermittent bursts in the time series of these variables. Such bursts are driven by the large-scale dynamics, and thus can be expected to be associated with longer time scales.

Enstrophy and pseudo-dissipation autocorrelations are consistently higher than those of acceleration magnitude and dissipation, up to time lags at which all have become negligible. The closeness between pseudo-dissipation and enstrophy

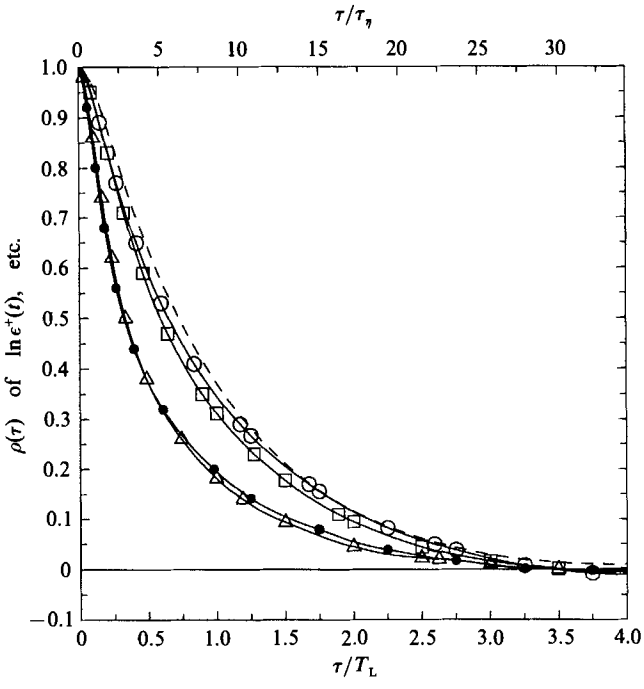

FIGURE 25. Same as figure 24, but for $\ln \epsilon^+(t)$, $\ln \zeta^+(t)$, $\ln \varphi^+(t)$ and $\ln |\boldsymbol{a}^+|(t)$.

autocorrelations can be explained by the strong effects of large enstrophy fluctuations on pseudo-dissipation. The integral timescale of enstrophy, T_ζ, is comparable with T_L, although T_ζ/T_L decreases with Reynolds number (see table 3).

Figure 25 shows the autocorrelations of the logarithms. It may be seen that they decay more slowly than those of the variables themselves. Comparison of tables 3 and 4 confirms that the logarithms have longer timescales. In proposing to model $\ln \varphi^+(t)$ as a UO process having an exponential autocorrelation function, Pope (1988*a*) has shown that the integral timescale of a UO process is always greater than that of its exponential. Under such assumptions the ratio of the respective integral timescales depends only on the variance of the UO process. Our results are qualitatively consistent with this predicted trend, but there are quantitative differences. The integral timescales of $|\boldsymbol{a}^+|(t)$ and $\ln |\boldsymbol{a}^+|(t)$ do not differ significantly. In figure 26, integral timescales of the logarithms, normalized by T_L, are shown against R_λ. The normalized timescales appear to decrease slightly with Reynolds number.

Frequency spectra for the three invariants at $R_\lambda = 93$ are shown in figure 27. To compare the relative contributions from different frequencies, each curve is normalized by the respective variance, with the velocity and acceleration spectra added for reference. With Kolmogorov scaling of frequency it is found that the curves change very little with Reynolds number. Clearly, the dissipation spectrum has a significantly greater proportion of high-frequency content than the enstrophy and pseudo-dissipation spectra. In turn, the latter two have more high-frequency content than the velocity spectrum, but the differences are smaller.

The above observations are entirely consistent with the already observed finding that the characteristic timescales are relatively short for ϵ^+, but comparable with T_L for ζ^+ and φ^+. Moreover, as may be expected from a comparison of the autocorrelations (figures 24 and 25), the corresponding spectra for the logarithms

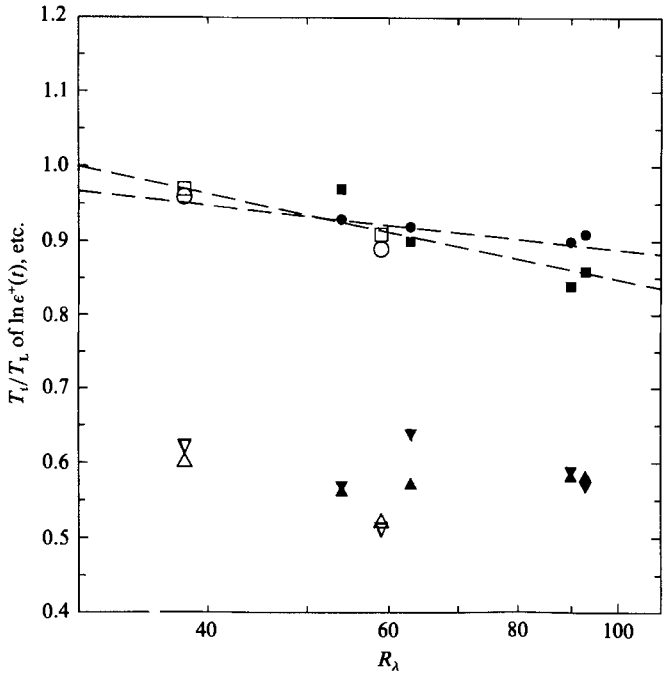

FIGURE 26. Integral timescales (T_i) of $\ln\epsilon^+(t)$, $\ln\zeta^+(t)$, $\ln\varphi^+(t)$, and $\ln|\boldsymbol{a}^+|(t)$, normalized by the Lagrangian integral timescale T_L, against R_λ. Symbols same as figure 20. Dashed lines indicate approximate Reynolds-number dependence for $\ln\zeta^+(t)$ and $\ln\varphi^+(t)$. No systematic variation for $\ln\epsilon^+(t)$ and $\ln|\boldsymbol{a}^+|(t)$ is evident.

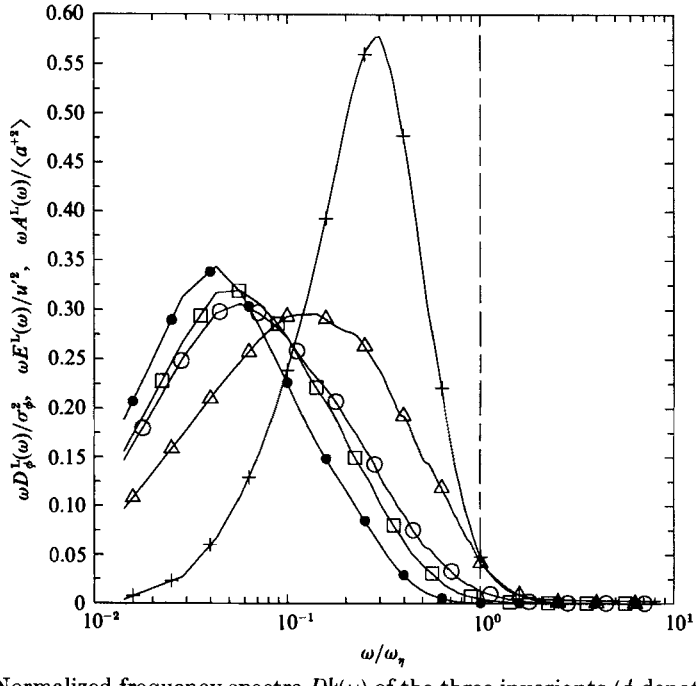

FIGURE 27. Normalized frequency spectra $D_\phi^L(\omega)$ of the three invariants (ϕ denoting ϵ^+, ζ^+ or φ^+) for the 128^3, $R_\lambda = 93$ simulation, shown against Kolmogorov-scaled frequency (at vertical dashed line). Each spectrum is normalized by the variance of the respective variable. △, ϵ^+; □, ζ^+; ○, φ^+. Normalized velocity (●) and acceleration (+) spectra also given for reference.

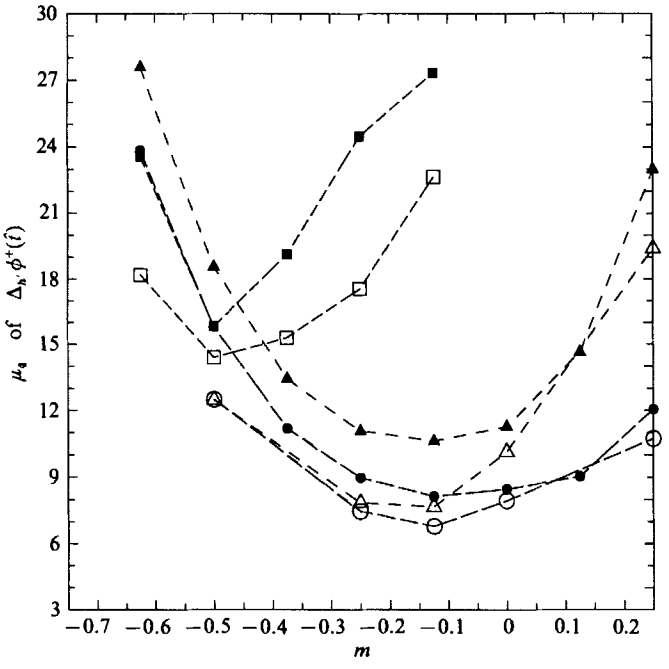

FIGURE 28. Flatness factors of increments of the invariants at smallest time lag (h') in stretched time, against the time-stretching exponent (m), for the 128^3, $R_\lambda = 63$ (open symbols) and $R_\lambda = 90$ (solid symbols) simulations. Each invariant is also the time-stretching variable. △, ϵ^+; □, ζ^+; ○, φ^+.

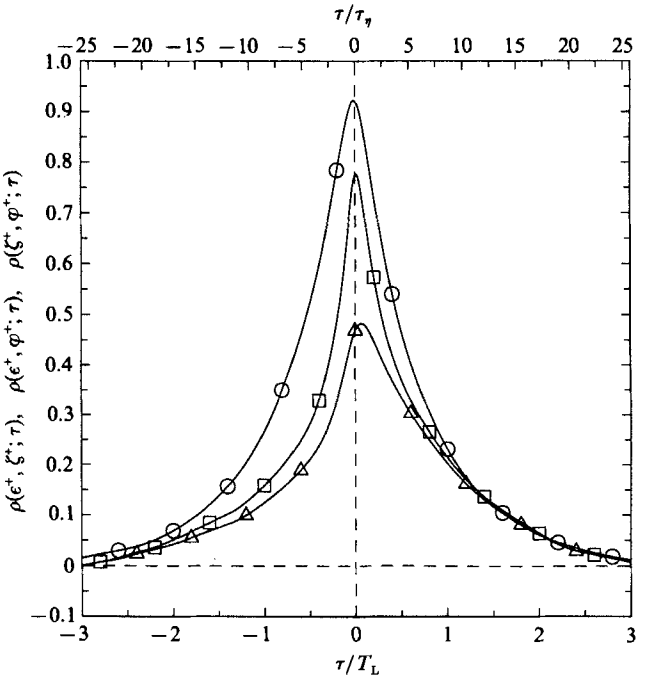

FIGURE 29. Cross-correlation functions among the invariants $\epsilon^+(t)$, $\zeta^+(t)$ and $\varphi^+(t)$, for the 128^3, $R_\lambda = 90$ simulation. Time lag is normalized by both T_L and τ_η. △, $\rho(\epsilon^+, \zeta^+; \tau)$; □, $\rho(\epsilon^+, \varphi^+; \tau)$; ○, $\rho(\zeta^+, \varphi^+; \tau)$. The cross-correlations are insignificant for time lags beyond the range shown.

(not shown) are shifted towards the lower frequencies. We also remark that for all three invariants the peak frequency ranges are lower than that of the acceleration, and that little contribution comes from frequencies higher than the Kolmogorov scale.

In §4.3 it is observed that the two-time statistics of velocity are made more nearly Gaussian by a local time stretching. Since $\ln\varphi^+$, and to a lesser extent $\ln\epsilon^+$ and $\ln\zeta^+$, are nearly Gaussian, it is natural to investigate their two-time statistics in stretched time $\hat{t}$, as defined by (27) (§4.1). Figure 28 shows the flatness factors of the increments of $\ln\epsilon^+(\hat{t})$, $\ln\zeta^+(\hat{t})$ and $\ln\varphi^+(\hat{t})$ for asymptotically small time intervals, for $R_\lambda = 63$ and 90 as functions of the scaling exponent m. In each case the invariant considered is also used as the scaling variable in (27). The flatness factors are seen to be lowest in the case of pseudo-dissipation. For $\ln\varphi^+(\hat{t})$, a minimum of about 7–8, with a small Reynolds-number dependence, occurs near $m = -\frac{1}{8}$, but is not much different from the regular time value (at $m = 0$) of about 8. By contrast, the increments of $\ln\zeta^+(\hat{t})$ are far from Gaussian for any m.

Figure 29 shows the two-time cross-correlation functions between the three invariants. The heights of all three curves reflect the relative magnitudes of the correlation coefficients (at zero time lag) given in table 5. The dissipation–enstrophy correlation is much stronger for enstrophy lagging behind dissipation ($\tau > 0$). This is consistent with the vortex-stretching effect: the vorticity of a fluid element subject to stretching (in the direction of ω) tends to increase with time.

To gain insight into the inter-relationship between spatial and temporal structures of the small scales, it is interesting to study the cross-correlation functions between acceleration magnitude and the quantities $\epsilon^+(t)$, $\zeta^+(t)$ and $\varphi^+(t)$. As a fluid particle enters a (small) region of large local velocity variations, it seems likely that its velocity would undergo rapid changes, and thus the acceleration would be large (in magnitude). These correlations are thus expected to be substantial, and positive. Figures 30 and 31 show these correlation functions, as $R_\lambda = 38$ and $R_\lambda = 90$ respectively. All are nearly zero beyond about three Lagrangian integral timescales. The correlation coefficients at zero time lag, given in table 5, are seen to increase with Reynolds number. Peak values in the range 0.35–0.5 occur at very small positive time lags (one Kolmogorov scale or less).

By a conditional sampling technique (say, given the event of $\epsilon^+(t)$ exceeding $\langle\epsilon\rangle$), the relatively high values at small time lags are found to be mostly contributed by intermittent bursts in the time series of the variables. For dissipation, there is a curious secondary peak at a negative (i.e. acceleration lagging behind) time separation of about $2\tau_\eta$, whose contribution is felt between $-5\tau_\eta$ and $-\tau_\eta$. The physical meaning is not entirely clear, but this feature seems less pronounced at higher Reynolds numbers. Since it is found at a time lag scaling with τ_η, it is probably caused by the small scales.

The acceleration–enstrophy cross-correlation function is seen to be markedly asymmetric, being stronger for $\tau > 0$ (enstrophy lagging). This could be the result of fluid particles being accelerated towards regions of high vorticity in the flow. For $\tau < 0$, the effect of local straining on the fluid particle acceleration is apparently stronger than that of local rotation.

The behaviour of pseudo-dissipation is the result of interplay between dissipation and enstrophy contributions. In fact, using (20) and (21), we can derive the relation

$$\rho(|\boldsymbol{a}^+|, \varphi^+) = \frac{1}{2}\left[\frac{\sigma(\epsilon^+)}{\sigma(\varphi^+)}\rho(|\boldsymbol{a}^+|, \epsilon^+) + \frac{\sigma(\zeta^+)}{\sigma(\varphi^+)}\rho(|\boldsymbol{a}^+|, \zeta^+)\right] \tag{37}$$

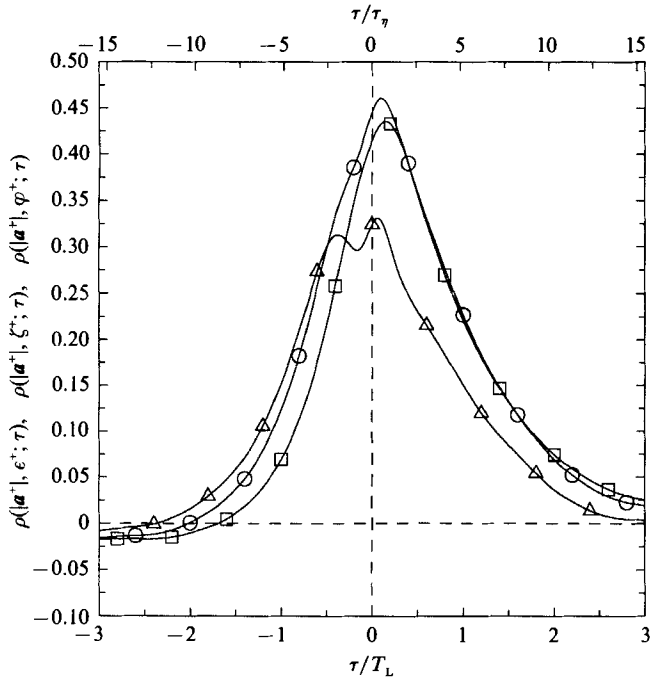

FIGURE 30. Cross-correlation functions between $|\boldsymbol{a}^+|(t)$ and the invariants $\epsilon^+(t)$, $\zeta^+(t)$ and $\varphi^+(t)$, for the 128^3, $R_\lambda = 38$ simulation. Time lag is normalized by both T_L and τ_η. $\triangle$, $\rho(|\boldsymbol{a}^+|, \epsilon^+; \tau)$; $\square$, $\rho(|\boldsymbol{a}^+|, \zeta^+; \tau)$; $\bigcirc$, $\rho(|\boldsymbol{a}^+|, \varphi^+; \tau)$. The cross-correlations are insignificant for time lags beyond the range shown.

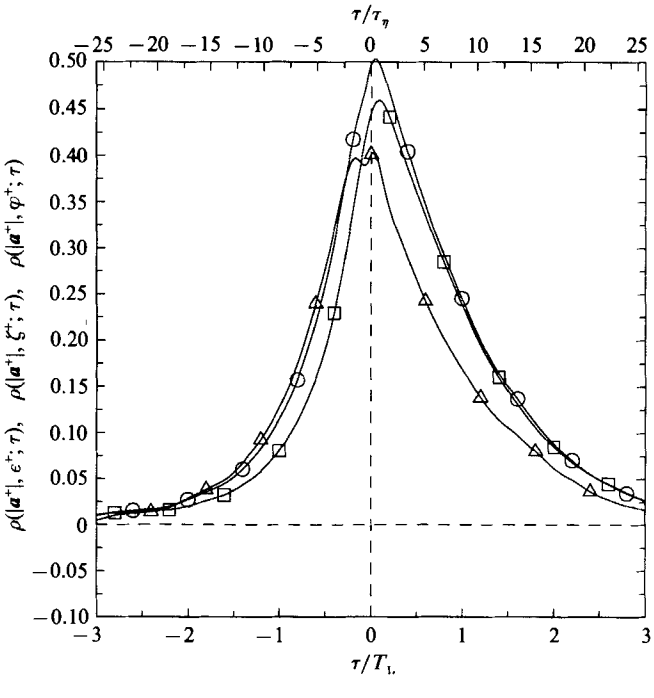

FIGURE 31. Same as figure 30, but for the 128^3, $R_\lambda = 90$ simulation.

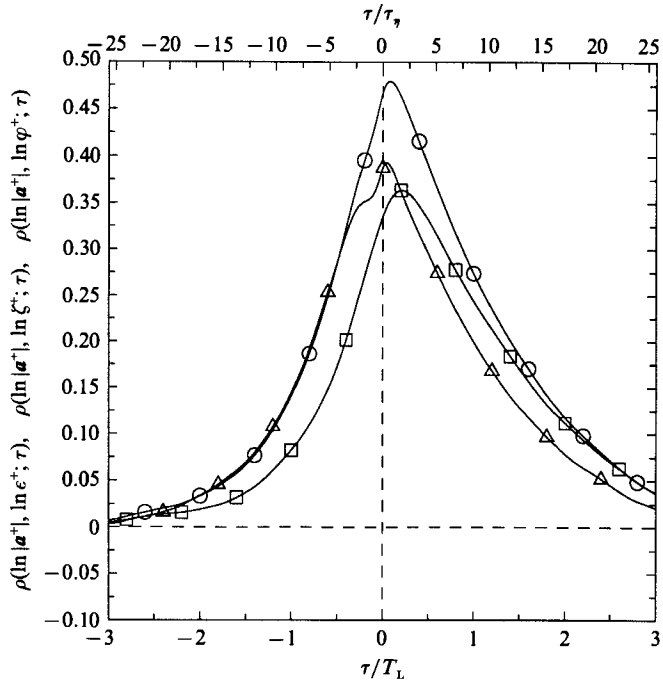

FIGURE 32. Same as figure 31, but for $\ln|\boldsymbol{a}|(t)$, $\ln\epsilon^+(t)$, $\ln\zeta^+(t)$ and $\ln\varphi^+(t)$.

(σ denotes standard deviation). That is, $\rho(|\boldsymbol{a}^+|, \varphi^+)$ is a weighted (by $\sigma(\epsilon^+)$ and $\sigma(\zeta^+)$) combination of $\rho(|\boldsymbol{a}^+|, \epsilon^+)$ and $\rho(|\boldsymbol{a}^+|, \zeta^+)$. Since enstrophy has a higher variance, $\rho(|\boldsymbol{a}^+|, \varphi^+)$ will always be closer to $\rho(|\boldsymbol{a}^+|, \zeta^+)$. In fact, table 5 indicates that $\rho(|\boldsymbol{a}^+|, \varphi^+)$ is the highest. When a time lag is considered, we find $\rho(|\boldsymbol{a}^+|, \varphi^+; \tau)$ to be consistently closer to the higher of $\rho(|\boldsymbol{a}^+|, \epsilon^+; \tau)$ or $\rho(|a^+|, \zeta^+; \tau)$.

Figure 32 shows $R_\lambda = 90$ data for the cross-correlation functions between the logarithms, such as $\rho(\ln|\boldsymbol{a}^+|, \ln\epsilon^+; \tau)$. A decrease in the small-time-lag range (compared with figure 31) is expected because bursts in the time series are much reduced on taking the logarithm. The secondary peak for pseudo-dissipation seen above becomes an inflection in the curve. Reduction of the correlation coefficient is greatest for enstrophy, since it is the most intermittent of the three invariants. We also note that the logarithms are not additive. Although the pseudo-dissipation correlation is still the result of contributions from dissipation and enstrophy, no simple relationship between the correlation coefficients for the logarithms is available.

4.5. *Relationship between Lagrangian and Eulerian time statistics*

There have been several attempts to relate Lagrangian statistics to Eulerian time statistics, since the latter are more readily measured (see, for example, Lumley 1962; Corrsin 1963; Hunt *et al.* 1987). In the following, Eulerian-time velocity statistics from the simulations are compared with Lagrangian data, and analysed in the context of the 'advection hypothesis' proposed by Tennekes (1975).

4.5.1. *Advection hypothesis, spectra and timescales*

Tennekes (1975) proposed to describe the temporal turbulence structure by an 'advection hypothesis'. Hunt *et al.* (1987) recently elaborated on the consequences.

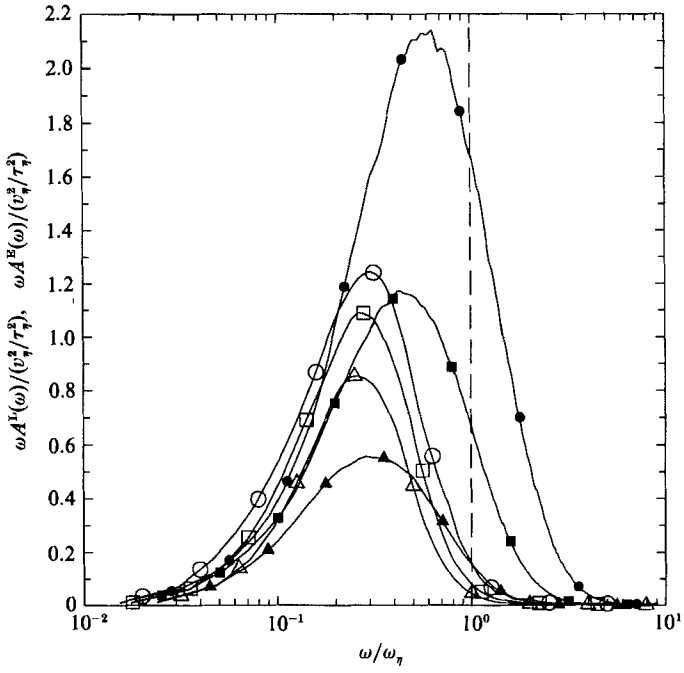

FIGURE 33. Scaled plots of frequency spectra of acceleration ($A^{\mathrm{L}}(\omega)$) and $\partial u/\partial t$ ($A^{\mathrm{E}}(\omega)$), against Kolmogorov-scaled frequency (at vertical dashed line) for 128^3 simulations. Area under each curve is the respective variance normalized by v_η^2/τ_η^2. Open symbols for $A^{\mathrm{L}}(\omega)$: △, $R_\lambda = 38$; □, $R_\lambda = 63$; ○, $R_\lambda = 90$. Solid symbols for $A^{\mathrm{E}}(\omega)$.

Applied to isotropic 'box' turbulence with no mean flow, Tennekes' basic argument is that the small dissipative eddies are advected, or swept, past a fixed observer by the large energy-containing eddies. This leads us to expect the Eulerian velocity frequency spectrum, denoted by $E^{\mathrm{E}}(\omega)$, to contain an appreciable fraction of energy for frequencies higher than the Kolmogorov frequency characterizing the smallest scales.

In our simulations, Eulerian frequency spectra are readily obtained from the time series of Eulerian velocity at a cubic lattice of 4096 fixed equispaced grid points. To bring out the differences between Lagrangian and Eulerian spectra, in figure 33 we show the scaled spectra of $\partial u/\partial t$, denoted by $A^{\mathrm{E}}(\omega)$ ($\equiv \omega^2 E^{\mathrm{E}}(\omega)$), and the acceleration spectra $A^{\mathrm{L}}(\omega)$ for Reynolds numbers from 38 to 90. It is readily seen that in contrast to the Lagrangian spectra, the Eulerian spectra do extend to frequencies considerably higher than the Kolmogorov scale ω_η ($\equiv \pi/\tau_\eta$). Moreover, the fraction of spectral content beyond ω_η appears to increase markedly with Reynolds number. These observations are consistent with the advection hypothesis.

Tennekes further assumed that at high Reynolds numbers, the dynamics of this advection effect can be analysed using a variant of Taylor's frozen turbulence approximation described below. For quantitative predictions, the experimental data of Comte-Bellot & Corrsin (1971) and Shlien & Corrsin (1974) were used to calculate proportionality constants in the model. Here we compare simulation results with the predictions and then examine Tennekes' analysis to explain the discrepancies.

The curves in figure 33 integrate to the respective component-averaged variances ($\langle(\partial u/\partial t)^2\rangle$ or $\langle(\mathrm{d}u^+/\mathrm{d}t)^2\rangle$), normalized by the Kolmogorov scales. These normalized variances are also given in table 6. In preceding sections we have seen that the

R_λ	38	63	90	93
Direct simulation (128^3) data				
$\dfrac{\langle a^{2+}\rangle}{v_\eta^2/\tau_\eta^2}$	1.38	1.87	2.32	2.28
$\dfrac{\langle(\partial u/\partial t)^2\rangle}{v_\eta^2/\tau_\eta^2}$	1.17	2.46	4.51	4.57
τ_L/τ_η	3.75	4.14	4.46	4.60
τ_E/τ_η	4.09	3.62	3.20	3.24
τ_L/τ_E	0.92	1.14	1.39	1.42
Estimates derived from Tennekes (1975)				
$\dfrac{\langle(\partial u/\partial t)^2\rangle}{v_\eta^2/\tau_\eta^2}$	3.27	5.42	7.75	8.00
τ_L/τ_η	9.97	12.83	15.34	15.59
τ_E/τ_η	2.45	2.45	2.45	2.45
τ_L/τ_E	4.07	5.24	6.26	6.36

TABLE 6. Velocity derivative variances and microscales

acceleration variance $\langle(\mathrm{d}u^+/\mathrm{d}t)^2\rangle$ does not obey Kolmogorov scaling in our Reynolds-number range. As for $\langle(\partial u/\partial t)^2\rangle$, Tennekes (1975) predicted

$$\langle(\partial u/\partial t)^2\rangle = \tfrac{1}{3}u'^2\frac{\langle\epsilon\rangle}{\nu}, \tag{38}$$

which is equivalent to

$$\frac{\langle(\partial u/\partial t)^2\rangle}{v_\eta^2/\tau_\eta^2} = \frac{R_\lambda}{3\sqrt{15}}. \tag{39}$$

The tabulated data show a rapid increase with Reynolds number, but are 40 to 65% less than the values based on (39).

In analogy with (23) which defines the Lagrangian microscale τ_L, the Eulerian time microscale τ_E is defined by

$$\tau_E = \left[\frac{2\langle u^2\rangle}{\langle(\partial u/\partial t)^2\rangle}\right]^{\frac{1}{2}}. \tag{40}$$

Tennekes' results predict τ_E/τ_η to be constant ($=\sqrt{6}$), but τ_L/τ_η to be proportional to $R_\lambda^{\frac{1}{2}}$, which is also true if acceleration variance scales according to Kolmogorov (1941) hypotheses – such that a_0 in (24) were strictly constant. The microscales are compared with the Kolmogorov timescale in table 6. Here the $R_\lambda = 90$ and 93 simulations differ little, suggesting that these results are relatively free from statistical errors. The ratios τ_L/τ_η, τ_E/τ_η and τ_L/τ_E are also shown in figure 34 as functions of Reynolds number, for both simulation and prediction. There is evidently extreme disagreement in the Lagrangian microscale. This calls for a close examination of the reasoning behind the theoretical estimates.

4.5.2. *Examination of Tennekes' (1975) analysis*

We begin with the fact that the material derivative of velocity, $\mathrm{D}\boldsymbol{u}/\mathrm{D}t$, is the local acceleration (of the fluid particle located instantaneously at a given point):

$$\frac{\mathrm{D}\boldsymbol{u}}{\mathrm{D}t} = \frac{\partial \boldsymbol{u}}{\partial t} + \boldsymbol{u}\cdot\nabla\boldsymbol{u} = \boldsymbol{a}. \tag{41}$$

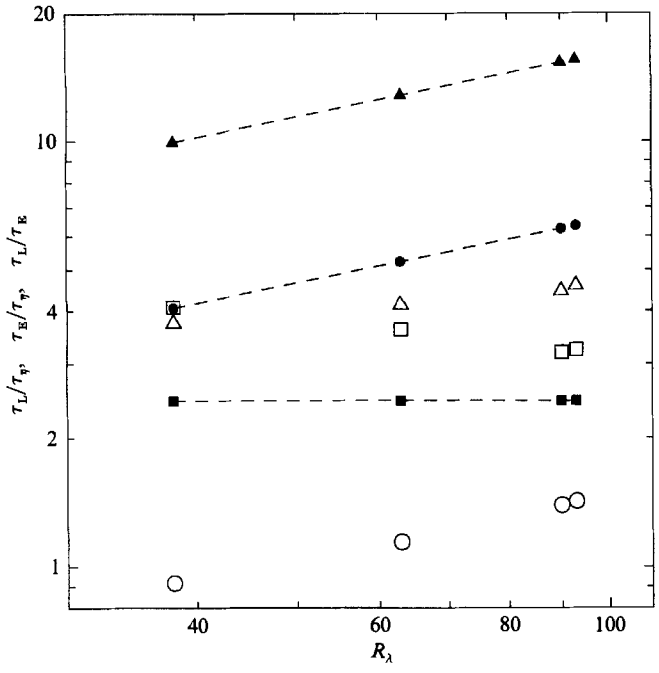

FIGURE 34. Calculated and predicted Eulerian and Lagrangian time microscale ratios against Reynolds number, for the 128^3 simulations. Open symbols for calculated values: △, τ_L/τ_η; □, τ_E/τ_η; ○, τ_L/τ_E. Predicted values (Tennekes 1975): solid symbols joined by dashed lines.

Taking expectations leads to

$$\left\langle \frac{\partial u_i}{\partial t}\frac{\partial u_i}{\partial t}\right\rangle = \left\langle u_k u_l \frac{\partial u_i}{\partial x_k}\frac{\partial u_i}{\partial x_l}\right\rangle - 2\left\langle a_i u_k \frac{\partial u_i}{\partial x_k}\right\rangle + \langle a_i a_i\rangle. \tag{42}$$

The major assumption in Tennekes' analysis is that Taylor's frozen turbulence approximation can be applied to the advection of small eddies by the large-scale motions. In effect, $\boldsymbol{a}$ is assumed to be negligible compared with the convective term, $\boldsymbol{u}\cdot\nabla\boldsymbol{u}$, and then (41) becomes

$$\frac{\partial \boldsymbol{u}}{\partial t} = -\boldsymbol{u}\cdot\nabla\boldsymbol{u}, \tag{43}$$

or, equivalently, $D\boldsymbol{u}/Dt = 0$. For convenience, we call (43) 'Tennekes' hypothesis'. The acceleration arises from the pressure and viscous terms in the momentum equation. The validity of the analysis thus rests on whether the neglect of such terms is indeed justified.

Tennekes also assumed $u_k u_l$ and $(\partial u_i/\partial x_k)(\partial u_i/\partial x_l)$ to be statistically independent, in view of the assumed separation (hence decoupling) between large and small scales. Hence (42) reduces to

$$\left\langle \frac{\partial u_i}{\partial t}\frac{\partial u_i}{\partial t}\right\rangle = \langle u_k u_l\rangle \left\langle \frac{\partial u_i}{\partial x_k}\frac{\partial u_i}{\partial x_l}\right\rangle. \tag{44}$$

In isotropic turbulence this further simplifies to

$$\left\langle \frac{\partial u_i}{\partial t}\frac{\partial u_i}{\partial t}\right\rangle = u'^2\frac{\langle\epsilon\rangle}{\nu}, \tag{45}$$

which in turn implies (38).

No. of terms	Algebraic form	$R_\lambda = 38$ (%)	$R_\lambda = 63$ (%)	$R_\lambda = 90$ (%)	$R_\lambda = 93$ (%)	Tennekes (1975) (%)
1	$\left\langle u_1^2\left(\frac{\partial u_1}{\partial x_1}\right)^2\right\rangle$	50.0	40.6	33.4	33.8	20.0
2	$\left\langle u_2^2\left(\frac{\partial u_1}{\partial x_2}\right)^2\right\rangle$	200.1	160.0	133.0	132.0	80.0
2	$\left\langle 2u_1u_2\frac{\partial u_1}{\partial x_1}\frac{\partial u_1}{\partial x_2}\right\rangle$	−20.2	−14.8	−9.6	−10.2	0
1	$\left\langle 2u_2u_3\frac{\partial u_1}{\partial x_2}\frac{\partial u_1}{\partial x_3}\right\rangle$	−20.5	−11.9	−7.6	−7.5	0
1	$\langle a_1^2\rangle$	117.5	76.7	51.3	49.8	0
1	$\left\langle 2a_1u_1\frac{\partial u_1}{\partial x_1}\right\rangle$	−41.9	−27.2	−17.9	−18.9	0
2	$\left\langle 2a_1u_2\frac{\partial u_1}{\partial u_2}\right\rangle$	−185.0	−123.4	−82.6	−75.8	0
	$\frac{\Sigma\lvert\text{neglected}\rvert}{\Sigma\lvert\text{retained}\rvert}$	1.540	1.270	1.018	0.978	0

TABLE 7. Percentage breakdown of contributions to the variance of $\partial u_1/\partial t$

To test Tennekes' assumptions leading to (45), we write (41) for one component of $\boldsymbol{u}$ as

$$\frac{\partial u_1}{\partial t} = -u_1\frac{\partial u_1}{\partial x_1} - u_2\frac{\partial u_1}{\partial x_2} - u_3\frac{\partial u_1}{\partial x_3} + a_1. \tag{46}$$

Invoking isotropy (so that, for example, the second and third terms on the right of (46) are statistically identical), the mean square of $\partial u_1/\partial t$ is given by

$$\left\langle\left(\frac{\partial u_1}{\partial t}\right)^2\right\rangle = \left\langle u_1^2\left(\frac{\partial u_1}{\partial x_1}\right)^2\right\rangle + 2\left\langle u_2^2\left(\frac{\partial u_1}{\partial x_2}\right)^2\right\rangle + 2\left\langle 2u_1u_2\frac{\partial u_1}{\partial x_1}\frac{\partial u_1}{\partial x_2}\right\rangle + \left\langle 2u_2u_3\frac{\partial u_1}{\partial x_2}\frac{\partial u_1}{\partial x_3}\right\rangle + \langle a_1^2\rangle - \left\langle 2a_1u_1\frac{\partial u_1}{\partial x_1}\right\rangle - 2\left\langle 2a_1u_2\frac{\partial u_1}{\partial x_2}\right\rangle. \tag{47}$$

If the small scales were uncorrelated with the large scales, then in (47) we would have

$$\left\langle u_1^2\left(\frac{\partial u_1}{\partial x_1}\right)^2\right\rangle = \langle u_1^2\rangle\left\langle\left(\frac{\partial u_1}{\partial x_1}\right)^2\right\rangle \tag{48}$$

(similarly for the 'transverse' term), and, since the Reynolds shear stress is zero here,

$$\left\langle 2u_1u_2\frac{\partial u_1}{\partial x_1}\frac{\partial u_1}{\partial x_2}\right\rangle = \left\langle 2u_2u_3\frac{\partial u_1}{\partial x_2}\frac{\partial u_1}{\partial x_3}\right\rangle = 0. \tag{49}$$

All the terms in (47) are one-point, one-time statistical moments, for which the Eulerian and Lagrangian p.d.f.'s are the same in incompressible homogeneous turbulence. They can therefore be calculated from the Lagrangian time series of velocity, acceleration and velocity gradients (in fact, moments involving the acceleration can only be obtained from Lagrangian data). Table 7 shows the relative contributions of each term on the right of (47) as a percentage of the left, after averaging over the coordinate directions. Also shown are the sizes ascribed to each

term by Tennekes' hypothesis (through the neglect of $\boldsymbol{a}$ with (48) and (49)). The bottom line gives the ratio of the sums of the magnitudes of the terms neglected by Tennekes to the ones retained. As in table 6, the $R_\lambda = 90$ and 93 results agree closely. Evidently, the terms involving acceleration are, in particular, far from negligible, showing that Tennekes' hypothesis is not applicable in the simulated Reynolds-number range. On the other hand, (48) and (49) are seen to be fair approximations.

We note that the discrepancy between simulation and prediction reduces steadily with increasing Reynolds number. Tennekes' hypothesis can be expected to hold at sufficiently high Reynolds numbers, but must be considered to be unsatisfactory for $R_\lambda = 93$ or less.

Tennekes used experimental data at $R_\lambda \approx 70$ (Comte-Bellot & Corrsin 1971) to evaluate numerical coefficients. However, our data show that even at $R_\lambda = 93$, his hypothesis appears unjustified. Thus presumably it does not apply to the experimental data either. Consequently, there is no reason to believe Tennekes' numerical results to be valid in general, even at Reynolds numbers high enough for his arguments to hold.

In view of (40), the above analysis of $\langle(\partial u/\partial t)^2\rangle$ suffices to explain the observed discrepancy in the Eulerian microscale. For the Lagrangian microscale, Tennekes' estimates depend heavily on the assumption of an extensive inertial frequency subrange satisfying Kolmogorov similarity. Again, the measurements of Shlien & Corrsin (1974) at $R_\lambda \approx 70$ were used to calculate numerical coefficients, but this Reynolds number is apparently not high enough for the analysis to be valid. As remarked in preceding sections, even at $R_\lambda = 90$, our data provide no evidence of an inertial subrange.

To close this subsection, we stress that our results do not cast doubt on the physical soundness of the advection hypothesis proposed by Tennekes (1975) at high Reynolds numbers. However, his analysis used experimental data at a Reynolds number that is not high enough to support the assumptions of negligibility of acceleration and the existence of an inertial subrange.

4.5.3. *Time and space correlations*

The relationship among Eulerian time, Eulerian space and Lagrangian velocity correlations (and the respective integral scales) is not well-established (Hunt *et al.* 1987). Although these correlations are readily obtained from the simulations, unfortunately artificial forcing precludes a faithful representation of the correlations at long time or space separations. This is because the forcing scheme feeds energy directly to the large and low-frequency scales accounting for substantial correlations at long separations.

Figure 35 shows the correlations obtained from the $R_\lambda = 63$ simulation, with spatial separations normalized by the half-width of the box, $\frac{1}{2}L_0$. Time lag is converted to separation distance by multiplying by the r.m.s. velocity. The distorting effects of artificial forcing are especially striking for the Eulerian correlations. The Eulerian time autocorrelation $\rho_E(\tau)$ is appreciable over much longer time lags than its Lagrangian counterpart. As a result, the Eulerian integral timescale, denoted by T_E, is substantially (up to 50%) larger than the Lagrangian integral scale. Since the simulation length (T) is limited, T_E, being relatively large, is also subject to much statistical uncertainty. Hunt *et al.* (1987) found $T_E/(\Lambda/u')$ to be 1.5 at $R_\lambda = 48$. For our data, this ratio is slightly greater than unity.

The longitudinal and transverse space correlations also retain significant non-zero values at the maximum separation (i.e. at $r = \frac{1}{2}L_0$). The computed integral

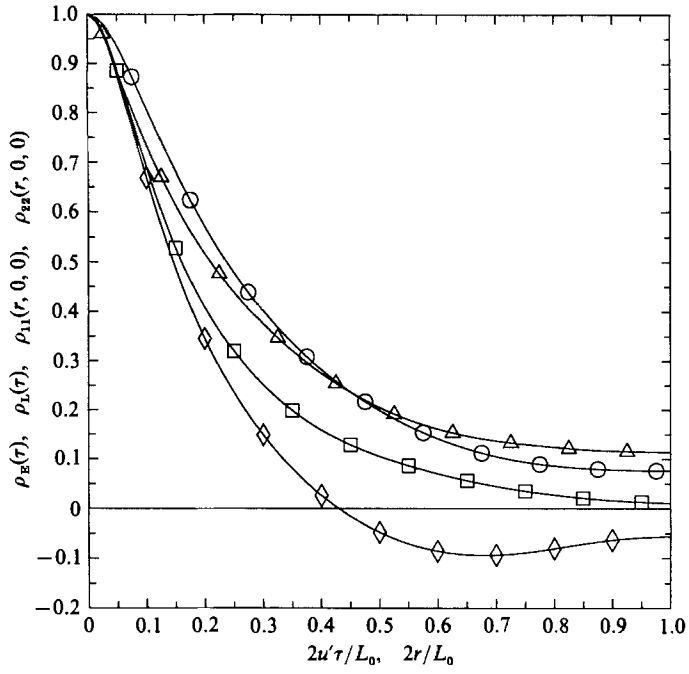

FIGURE 35. Four kinds of Eulerian and Lagrangian correlation functions, for the 128^3, $R_\lambda = 63$ simulation. Separation is measured as $2r/L_0$ or $2u'\tau/L_0$ (r is spatial separation, τ is time lag). △, $\rho_E(\tau)$; □, $\rho_L(\tau)$; ○, $\rho_{11}(r, 0, 0)$; ◇, $\rho_{22}(r, 0, 0)$.

lengthscales are thus inaccurate. The longitudinal lengthscale, L_1, deviates from the theoretical isotropic value of twice the transverse scale, L_2. Hunt *et al.* (1987) reported $L_1/L_2 = 1.64$, and attributed it to some degree of anisotropy of their forcing scheme.

5. Summary and conclusions

Direct numerical simulations of statistically stationary, homogeneous, isotropic turbulence have been performed, and Lagrangian time series have been extracted and analysed. The accuracy of the simulations has been demonstrated: the spatial and temporal resolution is excellent (with $k_{\max}\eta \approx 1.5$ and $C \approx 0.5$), and the use of cubic-spline interpolation makes the particle-tracking algorithm extremely accurate. Simulation durations of, typically, 5–6 eddy-turnover times are adequate to calculate most statistics, but some higher-order statistics suffer statistical sampling errors. To assess these errors, two statistically identical simulations are performed in selected cases.

Using 64^3 and 128^3 simulations, Taylor-scale Reynolds numbers in the range 38–93 have been achieved. The higher values $R_\lambda \approx 90$ are greater than those usually occurring in grid-generated turbulence, and are comparable with those found in the log-law region of a boundary layer at 270 wall units, or in an axisymmetric jet with a Reynolds number based on the pipe exit diameter of 7700. Nevertheless, the Reynolds number is too low for there to be a convincing separation between the energy-containing and dissipative scales. A $k^{-\frac{5}{3}}$ range is not observed in the Eulerian energy spectrum.

Because of the use of forcing and periodic boundary conditions, the large-scale motions most probably do not closely correspond to those of natural turbulence. But in this and previous studies it has been shown that the small scales are unaffected by forcing.

A major finding is that most of the Lagrangian statistics studied (normalized by the Kolmogorov scales) exhibit a strong Reynolds-number dependence. For example, a_0 (the acceleration variance normalized by the Kolmogorov scales) is found to increase approximately as $R_\lambda^{\frac{1}{2}}$ – increasing by 68% between $R_\lambda = 38$ and $R_\lambda = 90$ (figure 4). On the other hand, Eulerian statistics such as the dissipation spectra (figure 1) vary little with R_λ. Neither Kolmogorov's (1962) refined hypotheses, nor the more general local rescalings we considered, are successful in explaining the strong Reynolds-number dependence of a_0.

The acceleration frequency spectra (figure 11) do not exhibit the plateaus expected in the inertial range for high-Reynolds-number turbulence. Their peak values, B_0^*, increase as $R_\lambda^{\frac{1}{2}}$. The frequency spectrum of the Lagrangian velocity (figure 12) is affected little by the forcing or by Reynolds number, in marked distinction to the Eulerian wavenumber spectra (figure 2). Similarly the Lagrangian velocity autocorrelation functions differ little between the simulations; and, except near the origin, they resemble exponential decays.

For time lags τ up to four Kolmogorov timescales, the Lagrangian velocity increment $\Delta_\tau u^+(t)$ is found to be far from Gaussian: its standardized p.d.f., $p(v)$, decays as $\exp(-|v|)$ rather than as $\exp(-v^2)$ (figure 15); and flatness factors in excess of 10 are observed (figure 16).

The three velocity-gradient invariants studied show quite different statistical properties. The pseudo-dissipation $\varphi^+(t)$ (proportional to the second invariant of $\partial u_i/\partial x_j$, equation (18)) is found to be log-normal to within statistical uncertainty. On the other hand the dissipation $\epsilon^+(t)$ (equation (16)) and the enstrophy $\zeta^+(t)$ (equation (17)) are negatively skewed, indicating relatively high probabilities of low strain and rotation rates. The enstrophy is most intermittent, having a standard-deviation-to-mean ratio of about 1.5, compared to about 1.0 for ϵ^+ and φ^+. The correlation coefficient between $\ln\epsilon^+$ and $\ln\zeta^+$ is about 0.4 and increases with R_λ. When both $\ln\epsilon^+$ and $\ln\zeta^+$ are small, they appear to be statistically independent (figure 21).

The Lagrangian velocity integral timescale T_L is approximately $\frac{3}{4}$ of the eddy turnover time T_E (table 1). The integral timescales of $\ln\epsilon^+$, $\ln\zeta^+$ and $\ln\varphi^+$ are approximately $0.55T_L$, $0.9T_L$ and $0.9T_L$, respectively, with perhaps a weak decrease with R_λ. These large timescales for small-scale quantities arise because of internal intermittency: significant fluctuations in the dissipation, etc., occur on length- and timescales up to the integral scales. Autocorrelations (figures 24 and 25) and frequency spectra (figure 27) show that, compared with enstrophy and pseudo-dissipation, dissipation fluctuations are characterized by shorter timescales and higher frequencies.

The acceleration vector $\boldsymbol{a}^+(t)$ rotates on a timescale of order the Kolmogorov timescale τ_η: the zero-crossing time of the acceleration autocorrelations (figure 7) is about $2.2\tau_\eta$. But the integral timescale of the acceleration magnitude is about $0.6T_L$.

The Lagrangian data have been used to test Tennekes' (1975) advection hypothesis relating Lagrangian and Eulerian time derivatives. The hypothesis assumes high Reynolds number, and is found to be inaccurate at the moderate Reynolds numbers studied here.

The Lagrangian time series have been examined in the light of stochastic models such as the Langevin equation. It is found that the non-Gaussian velocity time series

$\boldsymbol{u}^+(t)$ can be made more nearly Gaussian by a time-stretching based on the pseudo-dissipation (figure 17). This corresponds to the variance of the velocity increments being proportional to the local pseudo-dissipation, rather than to the mean dissipation. Stochastic models for $\varphi^+(t)$ and $\boldsymbol{u}^+(t)$ based on these observations are described by Pope (1988*a*, *b*).

Perhaps the most striking finding in this paper is the strong Reynolds-number dependences of many of the Lagrangian statistics, and the inability of the refined Kolmogorov (1962) similarity hypotheses to account for them. It is of course true that the simulations are not at the very high Reynolds numbers required by the similarity hypotheses. But the Reynolds numbers are comparable with those of laboratory experiments. Hence our results provide a caution that applying high-Reynolds-number arguments to such measurements can lead to significant errors: the application of Tennekes' (1975) advection hypothesis to grid turbulence provides an example.

This work was supported by the US Air Force Office of Scientific Research (grant number AFOSR-85-0083). Computations conducted during the research were performed on the Cornell National Supercomputer Facility, which is supported in part by the National Scientific Foundation, New York State and the IBM Corporation.

The Lagrangian time series and other selected data have been recorded on magnetic tape. The contents of these tapes, and how they can be accessed, are described in the report by Yeung *et al.* (1988) which is available on request from the last author.

Appendix

In some of the simulations, especially those with only 18 forced modes (i.e. $K_F = \sqrt{2}k_0$), significant temporal variations of volume-averaged statistics are observed. For example, figures 36 and 37 show the volume-averaged dissipation and acceleration variance† for the 128^3 simulations. Up to 30% variations in dissipation, and 70% variations in acceleration variances may be seen, and are largest for the $R_\lambda = 90$ case. As might be expected, for each simulation these variations are in phase and highly correlated.

These observations raise several questions. First, are these variations a non-physical artifact of the forcing scheme, or are they found in natural turbulence? The answer lies between two suggestions. The solution domain is a cube of side approximately 5 integral lengthscales (table 1). In 'natural' turbulence – for example, that behind a turbulence-generating grid – if the volume-averaged dissipation were measured over a comparable volume, then temporal variations would certainly be observed. We cannot claim, however, that (in magnitude or timescale) the variations in the simulations match those of natural turbulence.

It is interesting to note that Siggia (1981) and Kerr (1985) used forcing schemes that are very different in this respect. Siggia deliberately used forcing that resulted in extremely large dissipation fluctuations, arguing that this is reflective of the intermittent nature of turbulence. Kerr, on the other hand, maintained constant energy in the forced modes and hence, presumably, the dissipation fluctuations were small. Our forcing scheme takes the middle ground.

† Where necessary, the volume average is estimated by averaging over all fluid particles at a given time.

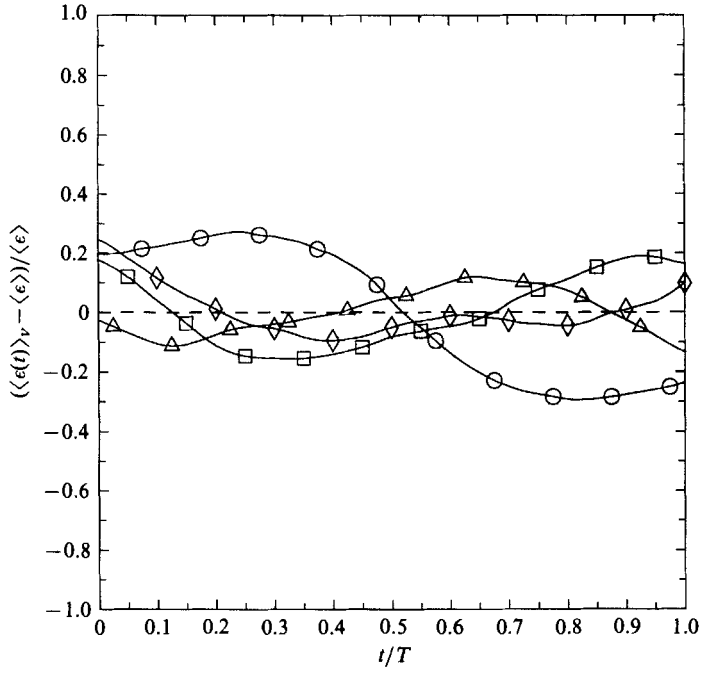

FIGURE 36. Temporal variation of volume-averaged dissipation, shown as normalized departure from the global mean, against time t normalized by the total integration time T (i.e. length of run), for the 128^3 simulations. △, $R_\lambda = 38$; □, $R_\lambda = 63$; ○, $R_\lambda = 90$; ◇, $R_\lambda = 93$.

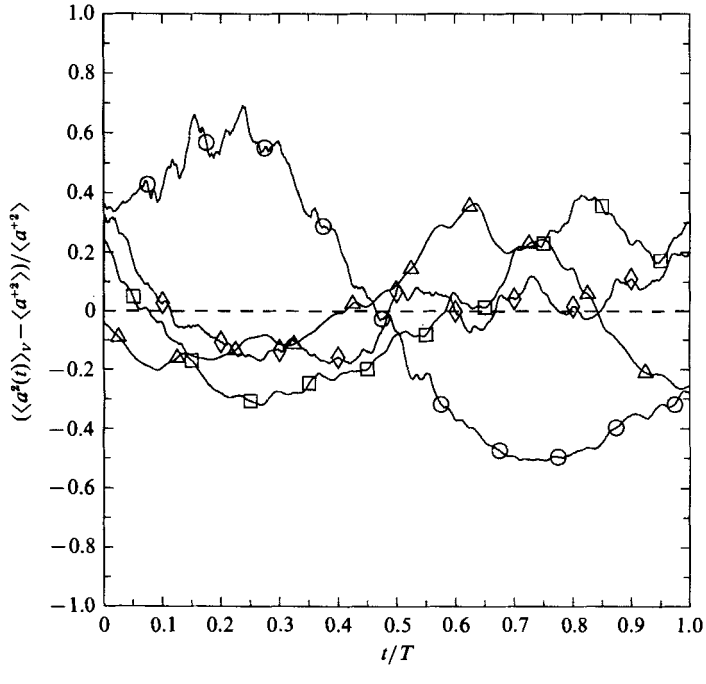

FIGURE 37. Temporal variation of volume-averaged acceleration variance, shown as normalized departure from the global mean, against time t normalized by the total integration time T for the 128^3 simulations. Symbols same as in figure 36.

The second question is: how do these variations affect statistical errors? Clearly, the effect may be large. For example, it may be seen from inspection of figure 37 that over the first half of the $R_\lambda = 90$ simulation time T the volume-averaged acceleration variance is typically 50% higher than over the second half. To be sure that the statistical errors are small, the sampling time T should be long compared with the observed time of variation, which is several eddy-turnover times. This requires a prohibitively large amount of computer time.

Because we cannot claim that the statistical errors are small, each simulation with $N_F = 18$ was performed twice (starting from different randomized initial conditions). That is, the $R_\lambda = 90$ and 93, and the $R_\lambda = 54$ and 59 simulations are statistically identical. For each statistic reported, a comparison of the values attained from each pair of runs affords an estimate of the sampling error.

In an attempt to reduce the sampling error, for some statistics the acceleration time series were preprocessed. Let $a^+(t)$ be the acceleration-component time series before preprocessing, $\langle a^2(t)\rangle_V$ be the time-dependent volume-averaged acceleration variance, and $\langle a^2\rangle$ be the time average of $\langle a^2(t)\rangle_V$ (i.e. $\langle a^2\rangle$ is the globally averaged acceleration variance). The preprocessing results in the modified time series $\hat{a}^+(t)$:

$$\hat{a}^+(t) \equiv a^+(t)\left[\frac{\langle a^2\rangle}{\langle a^2(t)\rangle_V}\right]^{\frac{1}{2}}. \tag{A 1}$$

Thus at all times the volume-averaged variance of $\hat{a}^+(t)$ is $\langle a^2\rangle$. The discussion of acceleration statistics in §4.1 implicitly assumes that preprocessed data are analysed.

This preprocessing does not alter the acceleration variance, but reduces its standard error. Similarly, other second-order statistics such as autocorrelations and frequency spectra are unaffected. However, it is found to reduce the higher-order moments, since large departures from the global mean are suppressed. At the smallest time lag (h), the velocity-increment flatness factor approximates that of the acceleration. Figure 38 shows, against R_λ, the acceleration-component flatness factors obtained both with (as in figure 6) and without (as in figure 16) preprocessing. Considerable scatter due to statistical variations is apparent. There is no clear theoretical reason to suggest which choice approximates the true acceleration flatness factor better. However, the $R_\lambda = 59$ and $R_\lambda = 90$ data in figure 38 appear to deviate considerably from the Reynolds-number trend suggested by all the simulations as a whole, suggesting the presence of considerable statistical errors in these two cases. The difference that preprocessing makes is especially large (between 13.3 and 17.8) for the $R_\lambda = 90$ case, suggesting that the $R_\lambda = 90$ curve in figure 16 is, on the whole, an over-estimation. By contrast, the $R_\lambda = 93$ curve, being only slightly above the $R_\lambda = 63$ curve, is possibly an under-estimation.

The large temporal variation of volume-averaged dissipation shown for the $R_\lambda = 90$ case in figure 36 makes the calculation of dissipation integral timescale T_ϵ inaccurate. From this figure it is evident that, because of this variation, dissipation fluctuations over long time lags (comparable with T) are likely to be negatively correlated. This is indeed observed, and leads to under-estimation of T_ϵ. To compensate for this statistical effect, integral timescales given in table 3 are computed from the preprocessed dissipation time series $\hat{\epsilon}^+(t)$, defined as follows. In analogy to (A 1), let $\langle\epsilon(t)\rangle_V$ and $\langle\epsilon\rangle$ be the volume and global averages of ϵ^+ respectively. Then $\hat{\epsilon}^+(t)$ is defined to be

$$\hat{\epsilon}^+(t) \equiv \epsilon^+(t)\frac{\langle\epsilon\rangle}{\langle\epsilon(t)\rangle_V}. \tag{A 2}$$

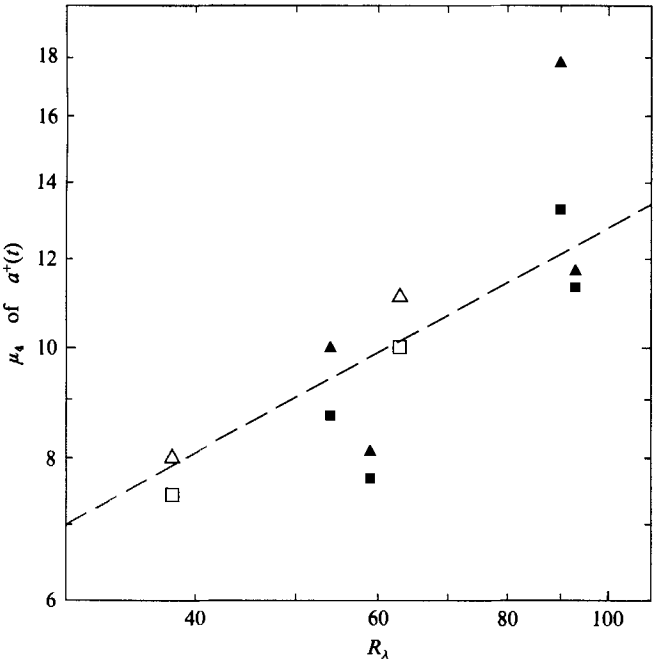

FIGURE 38. Acceleration-component flatness factors against Reynolds number, with (□) and without (△) the preprocessing described in the Appendix, for the same simulations as in figure 4. Open symbols for $K_F/k_0 = 2\sqrt{2}$, solid symbols for $K_F/k_0 = \sqrt{2}$. Dashed line of logarithmic slope $\frac{1}{2}$ indicate approximate Reynolds-number dependence.

The volume average of $\hat{\epsilon}^+(t)$ is $\langle\epsilon\rangle$ at all times. With this preprocessing, the dissipation autocorrelation is found not to take any significant negative values – being effectively zero at long time lags.

The same treatment is applied to the calculation of autocorrelations of the quantities $|\boldsymbol{a}^+|(t)$, $\zeta^+(t)$, $\varphi^+(t)$ and their logarithms, as well as the joint correlation functions between these variables. Small increases (of order 0.01) are found in the cross-correlation coefficients (table 5). We also note that the second and higher moments of $\epsilon^+(t)$ and $\hat{\epsilon}^+(t)$ differ. For the calculation of moments of $\epsilon^+(t)$ and $\ln\epsilon^+(t)$, preprocessing would be neither necessary nor appropriate.

Finally, we stress that the preprocessing described above is necessary only for simulations where relatively large temporal variations of volume-averaged of dissipation and acceleration variance are observed. Such variations are primarily associated with the use of $K_F = 2\sqrt{2}k_0$, affecting the 128^3, $R_\lambda = 90$, and also 64^3, $R_\lambda = 54$ and 59 simulations. In situations where the impact of these variations is small, acceleration and dissipation statistics computed with or without the preprocessing show only small differences. This is true for the $R_\lambda = 93$ case (apparently simply by chance), and the $R_\lambda = 38$ and 63 simulations made with $K_F = 2\sqrt{2}k_0$ (i.e. with greater number of forced modes).

Note added in proof. The observation, on p. 559, concerning scaling, is equivalent to that made from figure 6 in §4.1: namely that with $q = 1$, the acceleration in stretched time is – to a fair degree – approximately Gaussian. It should be noted that while the Kolmogorov (1962) hypotheses suggest the scaling $\Delta_\tau u^+ \approx (\epsilon\tau)^{\frac{1}{2}}$ for time

intervals τ in the inertial range, the results of figures 6 and 17 show that $\Delta_\tau u^+/(\varphi^+)^{\frac{1}{2}}$ can be considered approximately Gaussian even for $\tau \ll \tau_\eta$.

REFERENCES

ANAND, M. S. & POPE, S. B. 1985 In *Turbulent Shear Flows 4* (ed. L. J. S. Bradbury *et al.*), pp. 41–61. Springer.

ANAND, M. S., POPE, S. B. & MONGIA, H. C. 1989 In *Turbulent Reactive Flows*. Lecture Notes in Engineering, vol. 40, pp. 672–693: Springer.

ANSELMET, F., GAGNE, Y., HOPFINGER, E. J. & ANTONIA, R. A. 1984 *J. Fluid Mech.* **140**, 63.

ANTONIA, R. A., SATYAPRAKASH, B. R. & HUSSAIN, A. K. M. F. 1982 *J. Fluid Mech.* **119**, 55.

BASS, A. F. DE, DOP, H. VAN & NIEUWSTADT, F. T. M. 1986 *Q. J. R. Met. Soc.* **112**, 165.

COMTE-BELLOT, G. & CORRSIN, S. 1971 *J. Fluid Mech.* **48**, 273.

CORRSIN, S. 1963 *J. Atmos. Sci.* **20**, 115.

DOP, H. VAN, NIEUWSTADT, F. T. M. & HUNT, J. C. R. 1985 *Phys. Fluids* **28**, 1639.

ESWARAN, V. & POPE, S. B. 1988*a* *Computers Fluids* **16**, 257.

ESWARAN, V. & POPE, S. B. 1988*b* *Phys. Fluids* **31**, 506.

HANNA, S. R. 1981 *J. Appl. Met.* **20**, 242.

HAWORTH, D. C. & POPE, S. B. 1985 *Bull. Am. Phys. Soc.* **30**, 1694.

HAWORTH, D. C. & POPE, S. B. 1986 *Phys. Fluids* **29**, 387.

HAWORTH, D. C. & POPE, S. B. 1987 *Phys. Fluids* **30**, 1026.

HINZE, O. 1975 *Turbulence* (2nd edn). McGraw-Hill.

HUNT, J. C. R., BUELL, J. C. & WRAY, A. A. 1987 In *Proc. 1987 Summer Program*, pp. 77–94. Stanford-NASA Ames Center for Turbulence Research.

HUSSAINI, M. Y. & ZANG, T. A. 1987 *Ann. Rev. Fluid Mech.* **19**, 339.

KARLIN, S. & TAYLOR, H. M. 1981 *A Second Course in Stochastic Process*. Academic.

KERR, R. M. 1985 *J. Fluid Mech.* **153**, 31.

KOLMOGOROV, A. N. 1941 *Dokl. Akad. Nauk USSR* **30**, 299.

KOLMOGOROV, A. N. 1962 *J. Fluid Mech.* **13**, 82.

LEE, C. K., SQUIRES, K., BERTOGLIO, J.-P. & FERZIGER, J. H. 1987 Study of Lagrangian and Eulerian characteristic times using direct numerical simulation of turbulence. In *Proc. Sixth Symposium on Turbulent Shear Flows*, Toulouse, France.

LEE, M. J. & REYNOLDS, W. C. 1985 Numerical experiments on the structure of homogeneous turbulence. *Tech. Rep.* TF-24, Dept. of Mech. Engng, Stanford University.

LUMLEY, J. L. 1962 In *Mécanique de la Turbulence*, pp. 17–26. Centre National de la Recherche Scientifique, Paris.

MESTAYER, P. 1982 *J. Fluid Mech.* **125**, 475.

MONIN, A. S. & YAGLOM, A. M. 1971 *Statistical Fluid Mechanics*, vol. 1 (ed. J. L. Lumley). MIT Press.

MONIN, A. S. & YAGLOM, A. M. 1975 *Statistical Fluid Mechanics*, vol. 2 (ed. J. L. Lumley). MIT Press.

OBOUKHOV, A. M. 1962 *J. Fluid Mech.* **13**, 77.

ORSZAG, S. A. & PATTERSON, G. S. 1972 *Phys. Rev. Lett.* **28**, 76.

POPE, S. B. 1983 *Phys. Fluids* **26**, 404.

POPE, S. B. 1988*a* Stochastic model for Lagrangian dissipation. *Tech. Rep.* FDA-88-07, Sibley School of Mech. & Aero. Engng, Cornell University.

POPE, S. B. 1988*b* Stochastic model of Lagrangian velocity accounting for internal intermittency. *Tech. Rep.* FDA-88-11, Sibley School of Mech. & Aero. Engng, Cornell University.

PRIESTLEY, M. B. 1981 *Spectral Analysis and Time Series*. Academic.

REID, J. D. 1979 *Boundary Layer Met.* **16**, 3.

RILEY, J. J. & PATTERSON, G. S. 1974 *Phys. Fluids* **17**, 292.

ROGALLO, R. S. 1981 *Tech. Memo.* 81315. NASA Ames Research Center.

ROGALLO, R. S. & MOIN, P. 1984 *Ann. Rev. Fluid Mech.* **16**, 99.

ROGERS, M. M. & MOIN, P. 1987 *J. Fluid Mech.* **176**, 33.

SATO, Y. & YAMAMOTO, K. 1987 *J. Fluid Mech.* **175**, 183.

SCHLICHTING, H. 1979 *Boundary Layer Theory* (7th edn). McGraw-Hill.

SHLIEN, D. J. & CORRSIN, S. 1974 *J. Fluid Mech.* **62**, 255.

SIGGIA, E. D. 1981 *J. Fluid Mech.* **107**, 375.

SNYDER, W. H. & LUMLEY, J. L. 1917 *J. Fluid Mech.* **48**, 41.

TAVOULARIS, S. & CORRSIN, S. 1981*a* *J. Fluid Mech.* **104**, 311.

TAVOULARIS, S. & CORRSIN, S. 1981*b* *J. Fluid Mech.* **104**, 349.

TAYLOR, G. I. 1921 *Proc. Lond. Math. Soc.* (2) **20**, 196.

TENNEKES, H. 1975 *J. Fluid Mech.* **67**, 561.

TENNEKES, H. & LUMLEY, J. L. 1972 *A First Course in Turbulence*. MIT Press.

THOMSON, D. J. 1987 *J. Fluid Mech.* **180**, 529.

WARHAFT, Z. 1984 *J. Fluid Mech.* **14**, 363.

WARHAFT, Z. & LUMLEY, J. L. 1978 *J. Fluid Mech.* **88**, 659.

YEUNG, P. K., GIRIMAJI, S. & POPE, S. B. 1988 Eulerian and Lagrangian statistics from a high-resolution direct simulation of stationary homogeneous turbulence. *Tech. Rep.* FDA-88-02, Sibley School of Mech. & Aero. Engng, Cornell University.

YEUNG, P. K. & POPE, S. B. 1987 Lagrangian velocity statistics obtained from direct numerical simulations of homogeneous turbulence. In *Proc. Sixth Symposium on Turbulent Shear Flows*, Toulouse, France.

YEUNG, P. K. & POPE, S. B. 1988 *J. Comput. Phys.* **79**, 373.